IJMMM International Journal of Minerals, Metallurgy and Materials 矿物冶金与材料学报（英文版）

Cycling performance of layered oxide cathode materials for sodium-ion batteries

Jinpin Wu, Junhang Tian, Xueyi Sun, and Weidong Zhuang

Cite this article as:
Jinpin Wu, Junhang Tian, Xueyi Sun, and Weidong Zhuang, Cycling performance of layered oxide cathode materials for sodium-ion batteries, *Int. J. Miner. Metall. Mater.*, 31(2024), No. 7, pp. 1720-1744. https://doi.org/10.1007/s12613-023-2776-5

View the article online at SpringerLink or IJMMM Webpage.

INTERNATIONAL JOURNAL OF
Minerals, Metallurgy and Materials

Volume 31, Number 7, July 2024
Page 1720

Invited Review

https://doi.org/10.1007/s12613-023-2776-5

Cycling performance of layered oxide cathode materials for sodium-ion batteries

Jinpin Wu[1,2,3], *Junhang Tian*[1,2,3], *Xueyi Sun*[1,2,3)✉], *and Weidong Zhuang*[1,2,3)✉]

1) School of Metallurgical and Ecological Engineering, University of Science and Technology Beijing, Beijing 100083, China
2) State Key Laboratory of Advanced Metallurgy, University of Science and Technology Beijing, Beijing 100083, China
3) Beijing Key Laboratory for Green Recovery and Extraction of Rare and Precious Metals, University of Science and Technology Beijing, Beijing 100083, China
(Received: 14 August 2023; revised: 31 October 2023; accepted: 2 November 2023)

Abstract: Layered oxide is a promising cathode material for sodium-ion batteries because of its high-capacity, high operating voltage, and simple synthesis. Cycling performance is an important criterion for evaluating the application prospects of batteries. However, facing challenges, including phase transitions, ambient stability, side reactions, and irreversible anionic oxygen activity, the cycling performance of layered oxide cathode materials still cannot meet the application requirements. Therefore, this review proposes several strategies to address these challenges. First, bulk doping is introduced from three aspects: cationic single doping, anionic single doping, and multi-ion doping. Second, homogeneous surface coating and concentration gradient modification are reviewed. In addition, methods such as mixed structure design, particle engineering, high-entropy material construction, and integrated modification are proposed. Finally, a summary and outlook provide a new horizon for developing and modifying layered oxide cathode materials.

Keywords: sodium-ion battery; layered oxide materials; cycling performance; bulking doping; surface coating; concentration gradient; mixed structure; high-entropy

1. Introduction

The growing environmental problems caused by increasing fossil fuel consumption have gained considerable attention. Sustainable energy sources, such as wind, tide, water, and solar, have been exploited to mitigate the energy crisis and environmental pollution. These energy sources are regional, intermittent, and climatic, so developing electrical energy storage technology to provide continuous, controllable energy is a key link in sustainable energy applications [1]. Among these electrical energy storage technologies, lithium-ion batteries (LIBs) have been successfully commercialized in portable electronic devices and electric vehicles because of their high energy density and excellent cycling performance. However, the limited resources and uneven geographical distribution of lithium have raised concerns about cost and raw materials availability. Sodium-ion batteries (SIBs), with a similar "rocking chair" principle to LIBs, are considered an ideal complementary technology to LIBs because of the lower price and abundant reserves, suitable for electric vehicles and large-scale grids.

As a critical component of SIBs, cathode materials determine the electrochemical properties of SIBs. To achieve high performance for SIBs, various types of compounds have been studied as potential cathode materials, including layered oxides [2], polyanionic materials [3], and Prussian blue analogs. Layered oxides have been considered the most promising materials due to their high-capacity, high operating voltage, and simple synthesis. Layered oxides (Na_xTMO_2, TM = Mn, Fe, Ni, Co, Cr, V, Ti, Cu, etc.) can be mainly grouped as O-type and P-type according to Delmas's notations, as shown in Fig. 1(a) [4]. O and P represent Na ions occupying the octahedral (O) sites and trigonal prismatic (P) sites, respectively. The number after the letter refers to the repeating number of alkali-metal layers. For example, P2 means that Na ions occupy the P sites and the repeating number of Na ions layer is 2. Generally, layered oxides with a Na content in the range of $0.3 \leq x \leq 0.7$ show a P2 structure, while an increasing Na content trends to an O3 structure. The interactions between electrostatic cohesion force and electrostatic repulsive force change with Na content and show different interlayer distances. Thus, the ratio of ~1.62 between the distance of the Na layer and the distance of the transition metal layer has been used to distinguish P2 and O3-type structures [5]. On this basis, considering the extent of the cation electron density, the cation polarizability, and the ionic potential anion, Zhao *et al*. [6] proposed cation potential to elucidate the formation principle of different structures in layered oxides, and it is shown that small differences in TM or Na content will obviously lead to a phase structural change (Fig. 1(b)). In terms of cation potential, a high Na content represents a large mean Na ionic potential, which increases

✉ Corresponding authors: Xueyi Sun E-mail: sunxy@ustb.edu.cn; Weidong Zhuang E-mail: wdzhuang@ustb.edu.cn

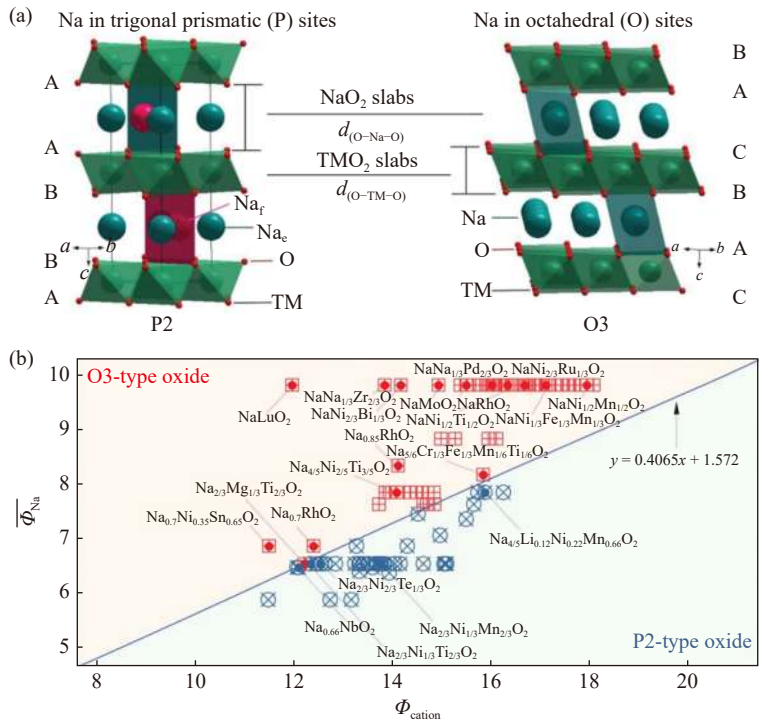

Fig. 1. (a) Schematic of the crystal structures for P2 and O-type layered oxides and (b) cationic potential and its use in Na-ion layered oxides ($d_{(O–Na–O)}$ and $d_{(O–TM–O)}$ refer to the interlayer distance of the Na metal layer and the TM layer, respectively. $\Phi_{cation} = \frac{\overline{\Phi_{TM}} \cdot \overline{\Phi_{Na}}}{\overline{\Phi_O}}$, refers to cationic potential, where $\overline{\Phi_{TM}}$ represents the weighted average ionic potential of TMs, $\overline{\Phi_O}$ represents the ionic potential anion, $\overline{\Phi_{Na}}$ represents the weighted average ionic potential of Na. Na_e and Na_f refer to the Na sites that share the faces with two TMO_6 octahedra and the Na sites that share only the edges with TMO_6 octahedra, respectively.) [6]. From C.L. Zhao, Q.D. Wang, Z.P. Yao, *et al.*, *Science*, 370, 708-711 (2020) [6]. Reprinted with permission from AAAS.

the shielding of the electrostatic repulsion between the TMO_2 slabs and results in the transformation from the P2 structure to the O3 structure. Cation potential is only suitable for predicting a single structure in one composition, not complicated situations, such as an entropy-dominated phase and disordered compounds resulting from mechanical milling.

In the past several decades, various layered oxides with a high specific capacity have been explored. O3-$NaMnO_2$, a typical single transition metal layered oxide, exhibited a discharge capacity of 185 mAh·g^{-1} between 2.0 and 3.8 V and a capacity retention of 71% after 20 cycles [7]. Electrochemical performance can be improved by partial substitution of Mn to form binary transition metal layered oxides. Komaba *et al.* [8–9] synthesized O3-$NaNi_{0.5}Mn_{0.5}O_2$ and P2-$Na_{2/3}[Fe_{1/2}Mn_{1/2}]O_2$. O3-$NaNi_{0.5}Mn_{0.5}O_2$ shows a capacity of 185 mAh·g^{-1} in the voltage range between 2.5 and 4.5 V. P2-$Na_{2/3}[Fe_{1/2}Mn_{1/2}]O_2$ material comprises only abundant and low price elements and delivers a discharge capacity of 190 mAh·g^{-1} with an average voltage of 2.75 V and a capacity retention of 73% over 30 cycles. Rong *et al.* [10] reported an anionic redox reaction of P2-$Na_{0.72}[Li_{0.24}Mn_{0.76}]O_2$, which shows a capacity of 270 mAh·g^{-1} and retains ~150 mAh·g^{-1} after 30 cycles in the voltage range between 1.5 and 4.5 V. Wang *et al.* [11] reported O3-$NaLi_{1/3}Mn_{2/3}O_2$, which delivers a reversible capacity of 190 mAh·g^{-1} by unlocking anionic redox and shows no discernible voltage fade over 40 cycles. In addition to the abovementioned layered oxides, a series of multi-transition metal oxides have been explored. Hwang *et al.* [12] designed P2-$Na_{0.55}[Ni_{0.1}Fe_{0.1}Mn_{0.8}]O_2$. It delivers a capacity of 221.5 mAh·g^{-1} in the voltage range of 1.5–4.3 V and shows capacity retention of 75% after 100 cycles. Wu *et al.* [13] reported P2-$Na_{0.7}Li_{0.03}[Mg_{0.15}Li_{0.07}Mn_{0.75}]O_2$, which shows a capacity of 266 mAh·g^{-1}. Although the discharge capacity in partial materials improved substantially, the cycling performance remains an inevitable issue. As commercialized LIB cathode materials, lithium iron phosphate shows a capacity retention of 86% after 10000 cycles [14], and NCM523 shows a capacity retention of 77% after 5000 cycles [15]. Compared to these materials, the poor cycling performance of layered oxide materials severely limits the practical application of SIBs.

To improve the cycling performance of layered oxides, this review focuses on challenges, such as phase transitions, ambient stability, side reactions, and irreversible anionic oxygen activity. Strategies for better cycling performance are illustrated in this review: (1) bulk doping; (2) homogeneous surface coating; (3) concentration gradient modification; (4) mixed structure design; (5) particle engineering; (6) high-entropy construction; and (7) integrated modification. It is believed that this review will help researchers to solve the critical challenges of layered oxide cathode materials.

2. Challenges of layered oxide cathode materials during the cycling process

The cycling performance of layered oxide cathode materi-

als is mainly affected by phase transitions, side reactions between electrolyte/air and electrode material, and irreversible anionic oxygen activity. The phase transitions may lead to volume changes and particle cracks, and the structure after the phase transitions may be irreversible or partially reversible. The side reactions between the electrolyte and electrode material consumes the Na in the electrode and decreases circulating capacity. Exposed to the air, the cathode material reacts with oxygen, water, and carbon dioxide, destroying its original structure and forming harmful substances. Anionic oxygen activity contributes to the capacity at high voltage, but the irreversible oxygen loss will lead to severe capacity decay and limited cycling stability. Understanding the challenges faced by the layered oxide cycle process can be targeted to modify the cathode material to obtain longer lifetimes. Challenges, including the phase transitions, side reactions between electrolyte and electrode, the effect of air on the cathode material, and irreversible anionic oxygen activity, will be described in detail below.

2.1. Phase transitions

In the process of charge and discharge, with the intercalation and deintercalation of sodium ions, the cathode material gradually forms different phases, and the irreversible phase transition and its associated volume changes will harm cycling performance. *Ex-situ* X-ray diffraction (XRD) spectra reveal the phase transition of P2-$Na_{0.67}Ni_{0.15}Fe_{0.2}Mn_{0.65}O_2$. The structure change from hexagonal P2 to O2 occurs in the process of charging at a working platform of 3.7 V, but the characteristic peaks of O2 still exist at the end of discharge, indicating the irreversible phase transition from P2 to O2 [16]. In the phase evolution of P2-$Na_{2/3}(Fe_{1/2}Mn_{1/2})O_2$ during charge and discharge, shown in Fig. 2(a), initial P2-$Na_{2/3}(Fe_{1/2}Mn_{1/2})O_2$ shows a hexagonal phase with a *Cmcm* space group [17]. Upon charging, P2-$Na_{2/3}(Fe_{1/2}Mn_{1/2})O_2$ maintains a hexagonal phase during the Mn^{3+}/Mn^{4+} transition and a solid solution-like two-phase reaction at 4.1 V. The P2 hexagonal phase forms an OP4 phase during the Fe^{3+}/Fe^{4+} transition when the voltage is higher than 4.1 V. Upon discharge, the OP4 phase transforms to the P2-type hexagonal phase and then returns to the P2-type hexagonal phase when the voltage is below 2.0 V. The volumes of three structures at 4.2, 2.7, and 1.5 V are 36.7, 41.6, and 42.9 $Å^3$, respectively. The ~12% volume change between the OP4 and P2 phases contributes to structural instability and poor cycling performance.

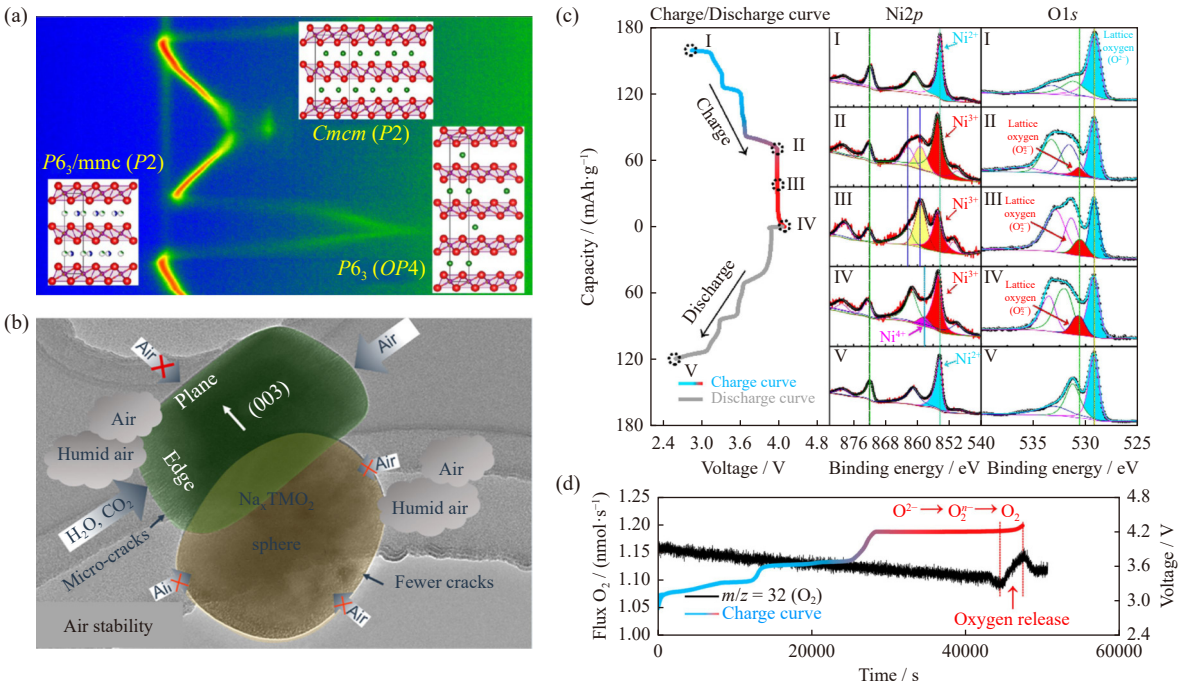

Fig. 2. (a) Phase evolution of P2-$Na_{2/3}(Fe_{1/2}Mn_{1/2})O_2$ during charge and discharge [17]. (b) Schematic of the side reaction when Na_xTMO_2 is exposed to the air [20]. (c) Galvanostatic charge/discharge curves of the $Na_{2/3}Ni_{1/3}Mn_{2/3}O_2$ electrode for the first cycle at 0.1 C and the corresponding XPS spectra of the Ni 2p and O 1s cores at various charge states and (d) *in situ* differential electrochemical mass spectrometry (DEMS) analysis of oxygen release during the first charge for the $Na_{2/3}Ni_{1/3}Mn_{2/3}O_2$ electrode [22]. (a) Reprinted with permission from W.K. Pang, S. Kalluri, V.K. Peterson, *et al.*, *Chem. Mater.*, 27, 3150–3158 (2015) [17]. Copyright 2015 American Chemical Society. (b) Reprinted with permission from C.L. Xu, H.R. Cai, Q.L. Chen, X.Q. Kong, H.L. Pan, and Y.S. Hu, *ACS Appl. Mater. Interfaces*, 14, 5338–5345 (2022) [20]. Copyright 2022 American Chemical Society. (c, d) Reprinted with permission from Y. Zhang, M.M. Wu, J.W. Ma, *et al.*, *ACS Cent. Sci.*, 6, 232–240 (2020) [22]. Copyright 2020 American Chemical Society.

2.2. Ambient stability and side reactions

Layered oxide cathode materials are sensitive to the H_2O and CO_2 in the air. The reaction between the electrode and H_2O/CO_2 generates a detrimental substance that deteriorates performance [18]. Take O_3-$NaNi_{0.7}Mn_{0.15}Co_{0.15}O_2$, for example. The characteristic (104) peak of O_3-$NaNi_{0.7}Mn_{0.15}Co_{0.15}O_2$ gradually fades and disappears with increasing ex-

posure time to air, while the characteristic peaks of Na_2CO_3, $Na_2CO_3·H_2O$, and NiO gradually appear and strengthen [19]. Xu *et al*. [20] kept the prepared O_3-$NaNi_{1/3}Fe_{1/3}Mn_{1/3}O_2$ in an oven at ~150°C to avoid air attack and then immediately transferred O_3-$NaNi_{1/3}Fe_{1/3}Mn_{1/3}O_2$ into a glovebox from the oven. However, a small diffraction peak is still observed at 12.70°, corresponding to the H_2O-intercalated hydrated phase. This trace hydrated phase indicates that O_3-$NaNi_{1/3}Fe_{1/3}Mn_{1/3}O_2$ is sensitive to H_2O molecules. The author also revealed that CO_2 inserts into Na layers along (003) planes and leads to Na_2CO_3 formation between adjacent TM layers, inducing fast structural degradation with surface cracks (Fig. 2(b)). In addition to the air attack, the trace amount of water reacting with $NaPF_6$ in the electrolyte generates HF, accelerating the dissolution of active metal ions [21]. Moreover, the dissolution of active metal ions accelerates electrolyte decomposition, finally leading to the decomposition of electrode materials and a deterioration of electrochemical performance.

2.3. Irreversible anionic oxygen activity

Anionic oxygen redox contributes to charge compensation at high voltages, while irreversible oxygen activity accelerates electrode material decomposition. Zhang *et al*. [22] studied the chemical evolution in $Na_{2/3}Ni_{1/3}Mn_{2/3}O_2$ by XPS analysis. As shown in Fig. 2(c), O_2^{n-} species occur at point II (charge to 4.2 V), corresponding to the emergence of the O 1s peak at 530.5 eV in the XPS spectra. From point I to point II (4.2 V), the O 1s peak intensity strengthens, indicating that more O_2^{n-} species participate in the electrochemical reaction at a high working voltage. The situ differential electrochemical mass spectrometry (DEMS) in Fig. 2(d) shows no O_2 generated when charged from the pristine state to 4.2 V, while O_2 suddenly increases when charged from 4.2 to 4.3 V. This irreversible evolution of $O^{2-}/O_2^{n-}/O_2$ leads to a sever capacity loss. Jiang *et al*. [23] revealed that surface cracks, active metal ions dissolution, and surface oxygen release combine to cause rapid capacity fading. House *et al*. [24] revealed that oxygen loss is not an inevitable consequence of a high working voltage and oxygen redox. No O or Mg is lost from $Na_{0.67}Mg_{0.28}Mn_{0.72}O_2$, even at 5 V, because oxygen is still coordinated with 2 Mn^{4+} and 1 Mg^{2+}. This coordination state ensures oxygen stays in bulk. In contrast, oxygen loss can be observed from $Na_{0.78}Li_{0.25}Mn_{0.75}O_2$ when the local coordination around oxygen is below 3. Thus, the author insists that oxygen loss is triggered when a high degree of alkali-ion deficiency leads to coordination around oxygen of less than 3.

3. Methods for improving cycling performance

To address the abovementioned challenges, many methods have been explored. Here, seven common methods are introduced: bulk doping, homogeneous surface coating, concentration gradient modification, mixed-phase designing, particle engineering, high-entropy material designing, and integrated modification.

3.1. Bulk doping

Bulk doping is the most widely used method for improving the performance of layered oxide materials. Here, we introduce bulk doping from three aspects: cationic single doping, anionic single doping, and multi-ion doping.

3.1.1. Cationic single doping

Lattice distortion caused by large lattice strain, abnormal bond length change, and anisotropic volume change leads to severe capacity fading in the cycling process caused by the Jahn–Teller effect of transition metals [25]. The influence of the Jahn–Teller effect on the material properties of layered oxides can be effectively mitigated by doping [26–27]. Cationic ions, including Nb^{5+}, Mo^{5+}, Sb^{5+}, Ti^{4+}, Al^{3+}, Cr^{3+}, B^{3+}, Mg^{2+}, Ca^{2+}, K^+, and Li^+, are commonly used in bulk doping [28–29]. Fang *et al*. [30] introduced the electrochemical inert ion B^{3+} at the interstitial site in $Na_{0.67}Fe_{0.5}Mn_{0.5}O_2$ to mitigate the Jahn–Teller effect. Mn K-edge X-ray absorption near edge structure (XANES) spectra during charge and discharge are shown in Fig. 3(a1) and (a2). Compared to NFMO-P, NFMO-B showed a considerably shift during charge process, indicating more Mn was involved in charge compensation. The edge peak of pristine NFMO-B appears considerably sooner than that of NFMO-P because the introduction of B^{3+} cations lowers the valence state of Mn to achieve charge balance. The extended X-ray-absorption fine structure (EXAFS) spectrum shows the Mn-O peak at 1.5 V of NFMO-B shifted from that of NFMO-P, indicating a lower valence state of Mn at low voltage after B^{3+} doping (Fig. 3(a3) and (a4)). The lower valence state of Mn can mitigate the Jahn–Taller effect and improve cycling performance. As the schematic illustration shown in Fig. 3(a5), the Mn e_g energy level splitting induced by the Jahn–Teller effect was mitigated by the introduction of B^{3+}. As shown in Fig. 3(a6), NFMO-B maintains a capacity of 114 mAh·g^{-1} in the voltage range of 1.5–4.0 V at 1 C after 100 cycles, a capacity retention of 89%. In contrast, the capacity retention of NFMO-P is only 64%, which is 24% lower than that of NFMO-B.

In addition to mitigating the Jahn–Teller effect, doping can improve internal structural stability. As a water-sensible material, P2-$Na_{0.67}Co_{0.20}Mn_{0.8}O_2$ (pristine) shows two water phase peaks near 12.6° and 25.4° when charged to 4.0 V because of abundant Na^+ deinterlace, leaving enough space for water molecules to embed. Yang *et al*. [31] synthesized Ce^{3+}-doped P2-$Na_{0.67}Co_{0.20}Mn_{0.79}Ce_{0.01}O_2$ (NCMC) through the solid-state method. The shrinkage of the TM–O bond length indicates a stronger electrostatic attraction between the transition metal ion and the oxygen ion, corresponding to the stronger Ce–O bond energy and improved structural stability. Meanwhile, the shorter Ce–O bond suppresses water molecule embedment into the sodium layer. Compared to the 70% capacity retention of the pristine sample at 1 C after 400 cycles, NCMC exhibits a capacity retention of 91.7% (Fig. 3(b1)). Doping ions function as a pillar and can also improve

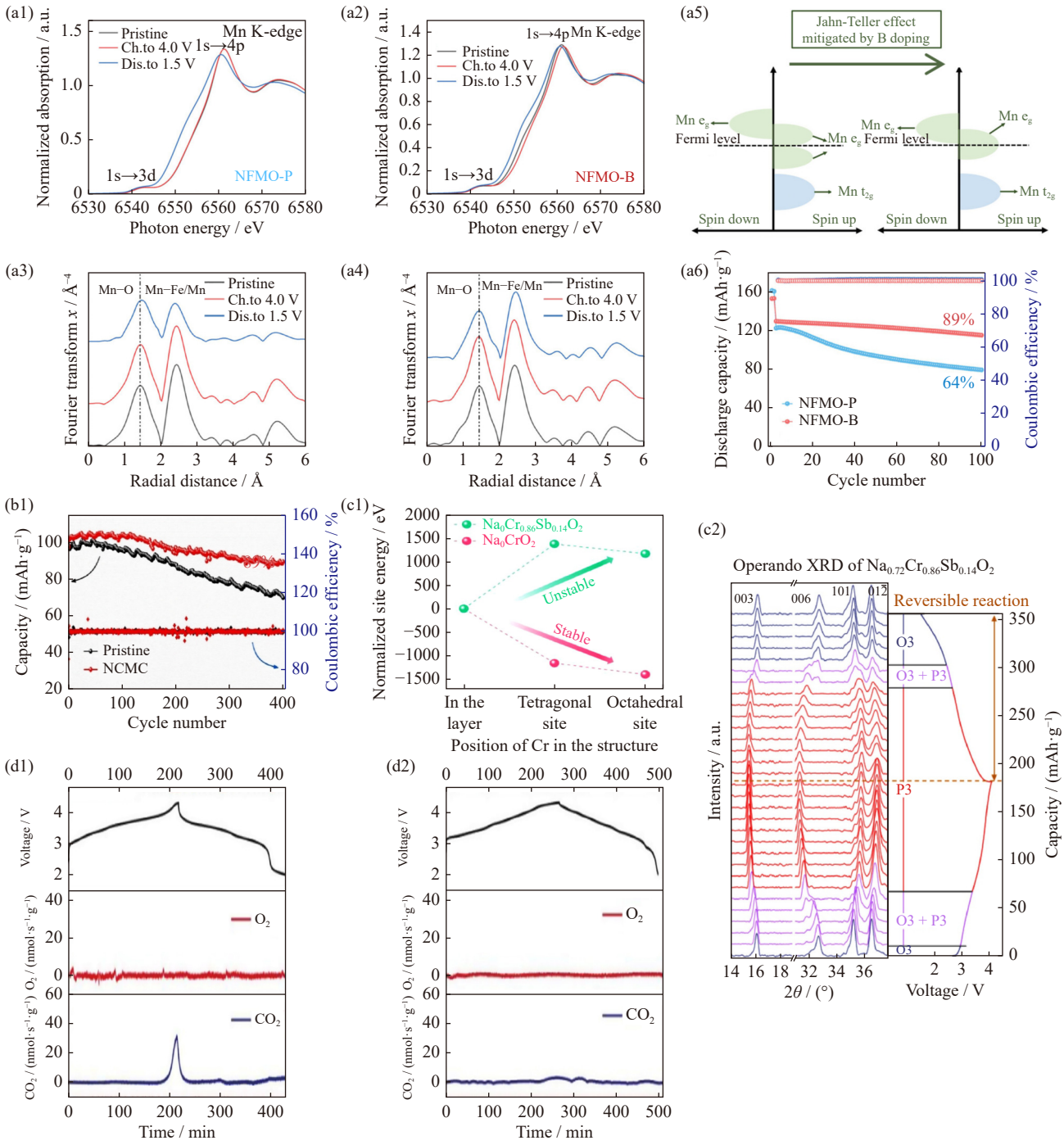

Fig. 3. ***Ex-situ*** **XANES spectra of the Mn K-edge at (a1) pristine, (a2) 4.0 V, and (a3) 1.5 V; EXAFS spectra of the Mn K-edge of (a4) NFMO-P and (a5) NFMO-B in different Na^+ extraction/insertion states; (a6) Cycling performance of the NFMO-P and NFMO-B cathodes at 1 C [30]. (b1) Cycling performances of pristine and NCMC at 1 C [31]. (c1) Formation energy as a function of the position of the chromium ion in O3-Na_0CrO_2 and O3-$Na_0Cr_{0.86}Sb_{0.14}O_2$; (c2) Operando XRD pattern of $Na_{0.72}Cr_{0.86}Sb_{0.14}O_2$ [37]. Gas release of (d1) P2-$Na_{0.67}Mn_{0.65}Ni_{0.2}Co_{0.15}O_2$ and (d2) P2-$Na_{0.67}Mn_{0.65}Ni_{0.2}Mg_{0.15}O_2$ during the initial cycle [38]. (a1–a6) H. Fang, H.C. Ji, J.J. Zhai, *et al*., *Small*, 19, 2301360 (2023) [30]. Copyright Wiley-VCH Verlag GmbH & Co. KGaA. Reproduced with permission. (b1) Reprinted from *J. Phys. Chem. Solids*, 148, X.H. Yang, Y.Z. Wang, J.L. Wang, J.Y. Deng, and X. Zhang, Superior cyclability of Ce-doped P2–$Na_{0.67}Co_{0.20}Mn_{0.80}O_2$ cathode for sodium storage, 109750, Copyright 2021, with the permission from Elsevier. (c1, c2) Reprint from *Energy Storage Mater*., 46, W. Ko, M.K. Cho, J. Kang, *et al*., Exceptionally increased reversible capacity of O3-type $NaCrO_2$ cathode by preventing irreversible phase transition, 289, Copyright 2022, with the permission from Elsevier. (d1, d2) Reprint from *Nano Energy*, 60, Y.F. Wen, J.J. Fan, C.G. Shi, *et al*., Probing into the working mechanism of Mg versus Co in enhancing the electrochemical performance of P2-Type layered composite for sodium-ion batteries, 162, Copyright 2019, with the permission from Elsevier.**

structural stability. Qin *et al*. [32] reported nonelectrochemical active Zn^{2+}-doped O3-$NaNi_{0.328}Mn_{1/3}Fe_{1/3}Zn_{0.005}O_2$ (NMF-Zn0.005), where Zn^{2+} serves as a pillar for the stable structure during the cycling process. The fewer cracks and in-

hibited oxygen loss at high voltages result in better cycling stability of NMF-Zn0.005, which exhibits a capacity retention of 86.53% after 200 cycles at 1 C. Moreover, doping can effectively inhibit irreversible phase transitions and transition metal migration and improve phase transition reversibility [33–36]. Ko *et al.* [37] reported Sb^{5+}-doped $Na_{0.72}Cr_{0.86}Sb_{0.14}O_2$, as shown in Fig. 3(c1). First-principles calculations indicate that Cr migration to Na layers is thermodynamically stable in Na_0CrO_2, while Cr migration to Na layers is thermodynamically unstable in $Na_0Cr_{0.86}Sb_{0.14}O_2$, illustrating that Cr will not prevent Na^+ diffusion in $Na_0Cr_{0.86}Sb_{0.14}O_2$. These results agree with the *ex-situ* XRD results, in which diffraction peaks, including (003), (006), (101), and (012), shift monotonically during the Na deintercalation/interaction process of $Na_0Cr_{0.86}Sb_{0.14}O_2$, indicating the reversible O3/P2 transition without O'3 phase formation (Fig. 3(c2)). Because of its high reversible phase transition, $Na_{0.72}Cr_{0.86}Sb_{0.14}O_2$ exhibits a capacity retention of 78.64% after 200 cycles at 2 C. The challenge from side reactions can also be mitigated by doping. Wen *et al.* [38] reported a complete replacement of Co with Mg in $Na_{0.67}Mn_{0.65}Ni_{0.2}Co_{0.15}O_2$. As shown in Fig. 3(d1) and (d2), compared to $Na_{0.67}Mn_{0.65}Ni_{0.2}Co_{0.15}O_2$, less CO_2 from electrolyte decomposition is detected in P2-$Na_{0.67}Mn_{0.65}Ni_{0.2}Mg_{0.15}O_2$ by an online DEMS test after Mg^{2+} doping, indicating that the side reaction between electrode and electrolyte is mitigated. The stable surface ensures a substantial improvement in capacity retention at 0.1 C over 100 cycles from 62% for $Na_{0.67}Mn_{0.65}Ni_{0.2}Co_{0.15}O_2$ to 94% for P2-$Na_{0.67}Mn_{0.65}Ni_{0.2}Mg_{0.15}O_2$.

In contrast to doping in transition metal sites, alkali ions, such as Li^+ and K^+, are usually introduced into Na sites [39–47]. Wang *et al.* [45] reported K-doped P2-$Na_{0.612}K_{0.056}MnO_2$, which exhibits a reversible capacity of 240.5 $mAh{\cdot}g^{-1}$, corresponding to an energy density of 654 $Wh{\cdot}kg^{-1}$. Fig. 4(a) and (b) shows the structure evolution during charge and discharge, in which P2-$Na_{0.612}K_{0.056}MnO_2$ shows only a reversible two-phase transition. The volume variation in P2-$Na_xK_{0.056}MnO_2$ is 7.8%, smaller than 11.2% for P2-Na_xMnO_2. A schematic partial density of states (pDOS) based on density functional theory (DFT) calculations shows

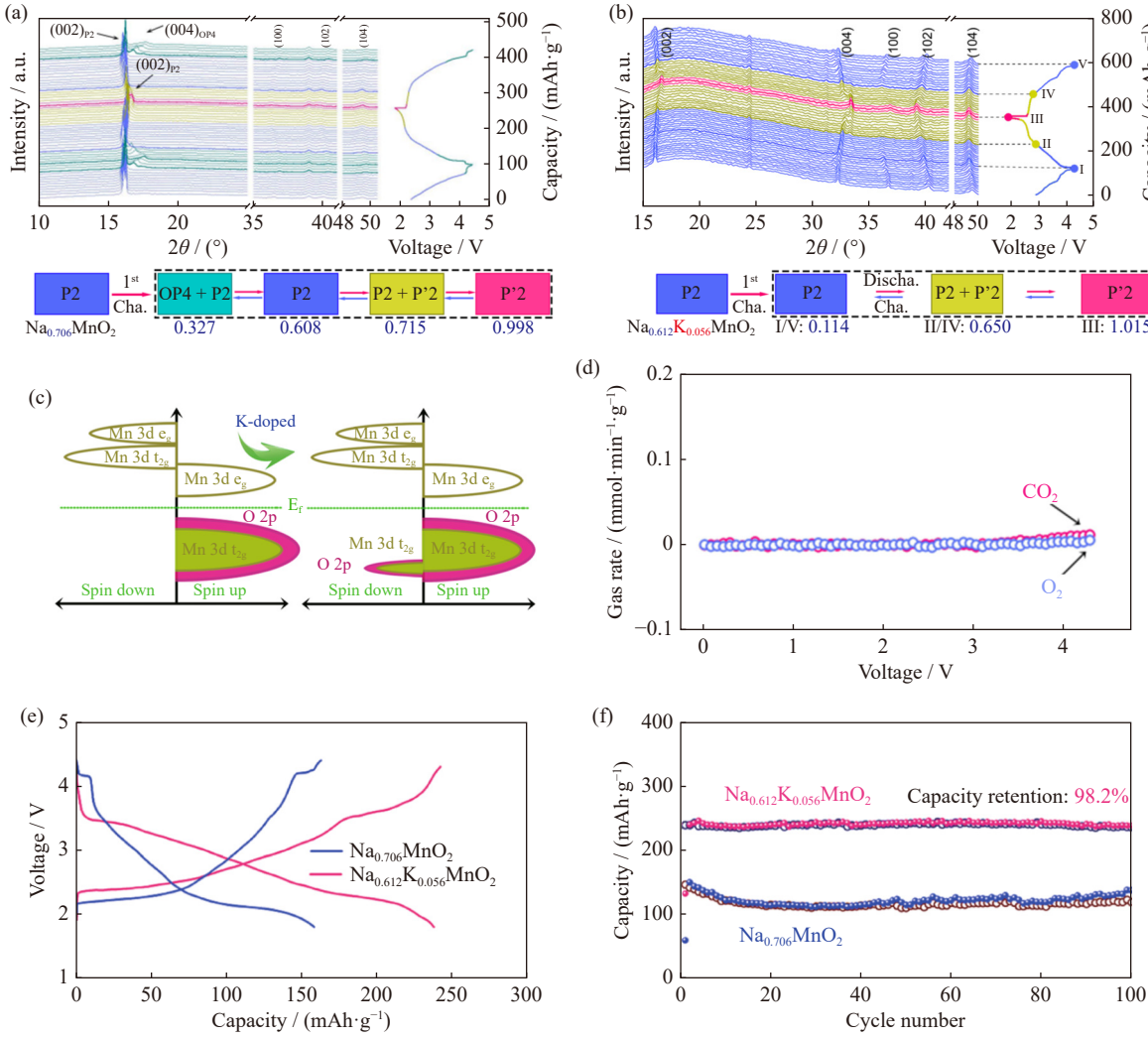

Fig. 4. ***In situ*** **XRD patterns and a schematic of the phase transitions of (a) $Na_{0.612}K_{0.056}MnO_2$ and (b) $Na_{0.706}MnO_2$. (c) Schematic pDOS of $Na_{0.555}MnO_2$ and $Na_{0.500}K_{0.055}MnO_2$. (d)** ***In situ*** **differential electrochemical mass spectrometry (DEMS) results of the gas evolution rates of CO_2 and O_2. (e) Charge/discharge curves of $Na_{0.612}K_{0.056}MnO_2$ and $Na_{0.706}MnO_2$ at 20 $mA{\cdot}g^{-1}$ in the third cycle. (f) Cycle performances of $Na_{0.612}K_{0.056}MnO_2$ and $Na_{0.706}MnO_2$ at 50 $mA{\cdot}g^{-1}$ [45].**

that spin-down electrons near the Fermi energy increase, indicating a stronger hybridization interaction between Mn and O after K^+ doping (Fig. 4(c)). Meanwhile, DEMS detects no oxygen evolution in the charging process in P2-$Na_{0.612}K_{0.056}MnO_2$ (Fig. 4(d)). The reinforced Mn–O bonds suppress the phase transition and improve the cycle stability during the charge/discharge process (Fig. 4(e)). As shown in Fig. 4(f), P2-$Na_{0.612}K_{0.056}$ MnO_2 exhibits a higher capacity retention of 98.2% after 200 cycles at 50 $mA·g^{-1}$, while the capacity retention of the pristine electrode fluctuates. In addition, Wu *et al*. [13] reported the dual-site doping in P2-$Na_{0.7}Li_{0.03}[Mg_{0.15}Li_{0.07}Mn_{0.75}]O_2$, in which Li ions substitute Na sites and transition metal sites. These two Li ions play different roles in P2-$Na_{0.7}Li_{0.03}$ $[Mg_{0.15}Li_{0.07}Mn_{0.75}]O_2$. Li_{NA} functions as a pillar that prevents the detrimental phase transformation and stabilizes the layered structure, whereas Li_{TM} forms Na–O–Li electronic configurations, which enhance the capacity derived from the oxygen anionic redox. P2-$Na_{0.7}Li_{0.03}[Mg_{0.15}Li_{0.07}Mn_{0.75}]O_2$ exhibits a specific capacity of 266 $mAh·g^{-1}$ in the voltage range of 1.5–4.6 V, and the capacity retention is 80.9% over 50 cycles at 0.5 C, compared to only 57.1% for the undoped cathode.

3.1.2. Anionic single doping

The anion site is an important part of the crystal structure. The anion F^- is usually introduced into an O^{2-} site to improve the cycle stability of a layered oxide [48]. Hu *et al*. [49] designed a substitution of partial O^{2-} ions with F^- ions in P2-$Na_{0.6}Mg_{0.3}Mn_{0.7}O_2$ (NMMO). P2-$Na_{0.6}Mg_{0.3}Mn_{0.7}O_{1.95}F_{0.05}$ (NMMOF5) exhibits a specific discharge of 205.5 $mAh·g^{-1}$, higher than 182 $mAh·g^{-1}$ for NMMO. As shown in Fig. 5 (a1), the higher oxidation peak of the dQ/dV curve in NMMOF5 indicates more oxygen redox reactions and cationic Mn redox reactions because of the stronger Na–F bond. A quantitative analysis of the Mn valence states based on the *ex-situ* Mn L-edge soft X-ray absorption spectroscopy (sXAS) spectra in total electron yield (TEY) mode is shown in Fig. 5(a2) and (a3). When discharging to 1.5 V, 63.53% Mn^{2+} is detected in NMMOF5, higher than 47.93% Mn^{2+} in NMMO. In other words, although Mn^{2+} shows high solubility in electrolytes, Mn^{2+} dissolution is suppressed after F^- doping because of the strong Mn–F bond. Meanwhile, 89.22% Mn^{4+} is detected in NMMOF5 when charging back to 4.5 V, which is near 88.93% in the pristine sample. A quantitative analysis indicates that the redox reaction between Mn^{2+} and Mn^{4+} is highly reversible, and the Jahn–Teller effect is effectively suppressed after F^- doping. Notably, excessive F^- harms electrochemical performance. As shown in Fig. 5(a4), NMMOF5 has a better cycling performance than NMMO, while NMMOF8 has a worse cycling performance than P2-NMMO. As mentioned above, the decrease in Mn^{3+} mitigates the Jahn–Teller effect and then improves electrochemical performance [50]. Interestingly, researchers have also reported that the Jahn–Teller effect can be suppressed by eliminating the Mn^{3+} high-spin state without decreasing Mn^{3+} content [51–54]. Kang *et al*. [55] revealed that more Mn^{4+} is reduced to Mn^{3+} with increasing F^- content, and the atomic ratio of Mn^{3+}/Mn^{4+} increases from 0.72 to 1.61 according to an analysis of Mn 2p spectra in Fig. 5(b1). Mn^{3+} disrupts the Ni^{2+}/Mn^{4+} cation ordering by occupying Ni^{2+} sites, which also suppresses the Jahn–Teller effect. Moreover, as shown in Fig. 5(b2), the ratio of surface oxygen/lattice oxygen decreases with increasing F^-, indicating more lattice oxygen participates in charge compensation, and the structural stability is improved after F^- doping. As shown in Fig. 5(b3) and (b4), F-0.05 not only shows higher rate capability but also maintains an impressive capacity retention of 78% after 900 cycles.

3.1.3. Multi-ion doping

To use the synergetic effect from different elements, multi-ion doping has been adopted to improve electrochemical performance [56–61]. Kubota *et al*. [62] studied quadrivalent ion (Ti^{4+}) and bivalent ion ($Cu^{2+}/Mg^{2+}/Zn^{2+}$) codoping $Na_{2/3}[Ni_{1/4}Mn_{1/2}Me_{1/12}Ti_{1/6}]O_2$ (Me = Mg, Cu, Zn). The Ti/Zn codoped sample shows a good cycling performance with almost no capacity loss over 40 cycles. This lower capacity degradation is due to smaller volume changes. The Ti/Zn codoped sample shows a smaller volume change of 7% compared to 13% for the Ti-doped sample and 23% for the undoped sample. Although the cycling performance and rate performance have been improved, the discharge capacity in the first cycle of these codoped samples decreases. Lee *et al*. [63] reported Ti/Ca codoped O3-$Na_{0.9}Ca_{0.035}Cr_{0.97}Ti_{0.03}O_2$. Ca doping leads to a stronger interaction between Ca^{2+} and O^{2-}, resulting in less volume expansion during the electrochemical reaction. Charge density calculations reveal that Ti^{4+} can attract more electrons and prevent the formation of unstable Cr^{4+}, suppressing Cr migration. This reinforced structural stability not only ensures good cycling performance (81.2% capacity retention after 1000 cycles at 10 C) but also ensures good performance in pouch cells, good thermal stability, and ambient stability. Zhang *et al*. [64] reported Li/Ti codoped $Na_{7/9}Li_{1/9}Ni_{2/9}Mn_{5/9}Ti_{1/9}O_2$ (LNMT), which exhibits a more stable structure and better electrochemical performance. Li^+ and Ti^{4+} can disorganize the NiMn ordering, and the Li/Ti codoping can maximize the disruption. The transition layers interact with Na layers, and the change after codoping can be reflected by the Na layers. As shown in Fig. 5(c1), the stable structure of LNMT can be explained by the Na^+ rearrangement mechanism. After Li/Ti introduction, a more thermodynamically stable Na_e site induces more Na^+ ions to occupy Na_e sites, leading to the rearrangement of Na^+ ions and a disruption of Na^+/vacancy ordering. This disruption decreases the formation energy in Na sites, corresponding to a more stable structure (Fig. 5(c2)). During the charging process, a newly ordered structure forms in $Na_{7/9}Ni_{1/3}Mn_{2/3}O_2$ (NM), hindering the Na^+ kinetic process. However, the structure remains disordered throughout the charging process in LNMT.

In addition to the multi-cationic ion codoping, cationic and anionic codoping are also adopted widely [16,65–66]. Zhou *et al*. [67] reported F/Ti codoped P2-$Na_{0.67}Ni_{0.33}Mn_{0.37}Ti_{0.3}O_{1.9}F_{0.1}$ (NaNMTi0.3OF), in which Ti-doping can disorganize Na^+/vacancy ordering, and F-doping can reduce po-

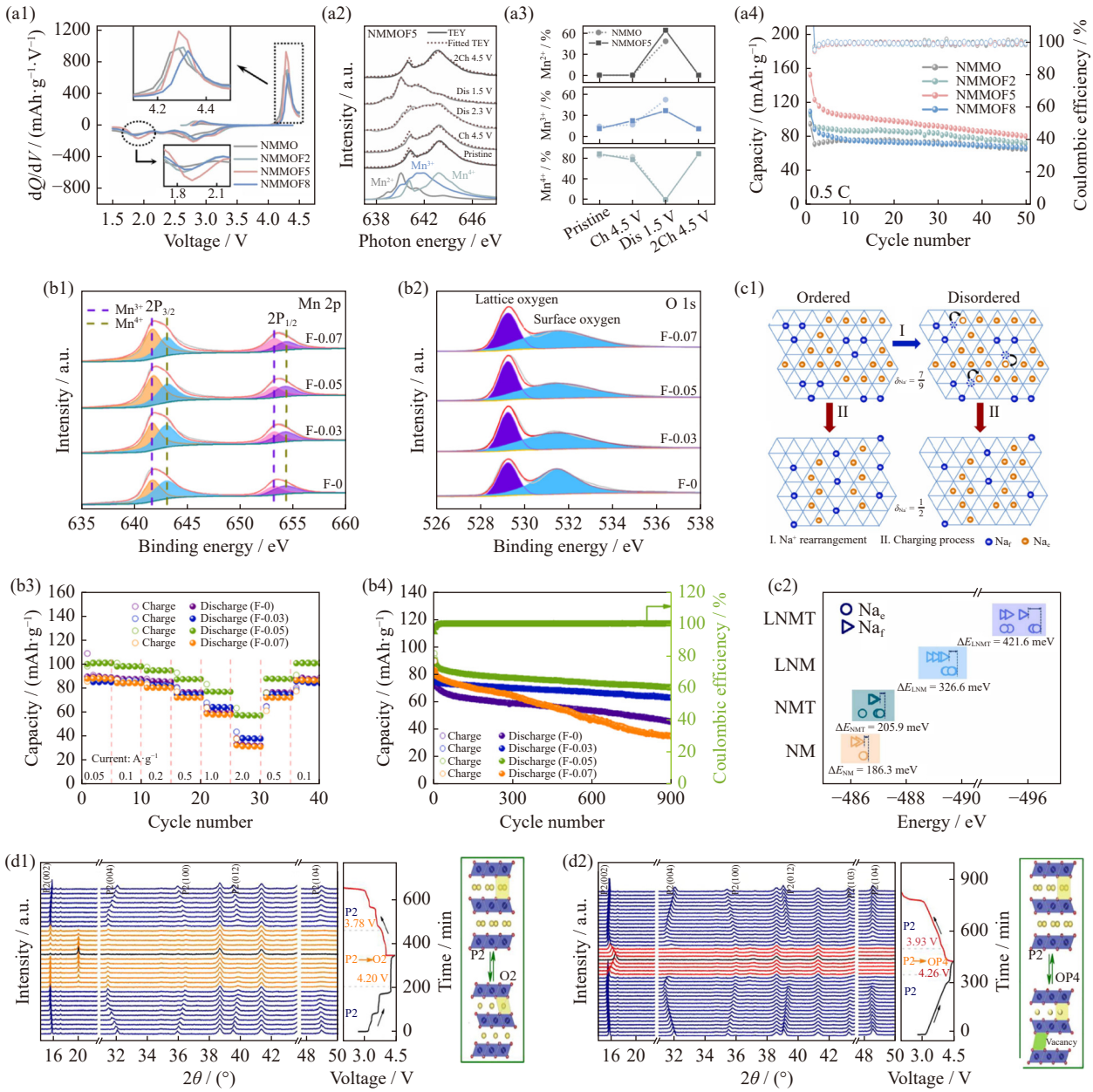

Fig. 5. (a1) d*Q*/d*V* curves of NMMO, NMMOF2, NMMOF5, and NMMOF8 at a current density of 0.05 C; (a2) Mn L-edge TEY spectra (solid lines) and fitted spectra (dashed lines); (a3) quantitative analysis of the valence state of Mn based on the fitting results; (a4) cycling performances of NMMO, NMMOF2, NMMOF5, and NMMOF8 in the voltage range of 1.5–4.5 V [49]. XPS patterns of the $Na_{0.6}Mn_{0.7}Ni_{0.3}O_{2-x}F_x$ samples of (b1) Mn 2p and (b2) O 1s. rate capability at different current densities (b3) and the cycling performances (b4) of different samples [55]. (c1) schematic of the process of Na^+ rearrangement; (c2) calculated formation energies of Na_c and Na_f sites (Na_c and Na_f refer to the Na sites that share the faces with two TMO_6 octahedra and the Na sites that share only the edges with TMO_6 octahedra, respectively.) [64]. *In-situ* XRD patterns of (d1) NaNMO and (d2) NaNMTi0.3OF during the first charge/discharge process [67]. (a1–a4) Reprint from *Nano Energy*, 99, H.L. Hu, H.C. He, R.K. Xie, *et al.*, Achieving reversible Mn^{2+}/Mn^{4+} double redox couple through anionic substitution in a P2-type layered oxide cathode, 107390. Copyright 2022, with permission from Elsevier. (b1–b4) Reprint with permission from W.P. Kang, P. Ma, Z.N Liu, *et al.*, *ACS Appl. Mater. Interfaces*, 13, 15333–15343 (2021) [55]. Copyright 2021 American Chemical Society. (c1, c2) Reprint from *Nano Energy*, 100, T.L. Zhang, H.C. Ji, X.H. Hou, *et al.*, Promoting the performances of P2-type sodium layered cathode by inducing Na site rearrangement, 107482, Copyright 2022 with permission Elsevier. (d1, d2) Reprint from *J. Energy Chem.*, 67, P.F. Zhou, J. Zhang, Z.N. Che, *et al.*, Insights into the enhanced structure stability and electrochemical performance of Ti^{4+}/F^- co-doped P2-$Na_{0.67}Ni_{0.33}Mn_{0.67}O_2$ cathodes for sodium ion batteries at high voltage, 655, Copyright 2021 with permission Elsevier.

larization. The P2–O2 phase transition is suppressed during the cycling process, as revealed by *in-situ* XRD measurements. As shown in Fig. 5(d1), charging NaNMO to 4.2 V generates the O2 phase, leading to a high energy barrier to Na^+ diffusion. In contrast, the O2 phase does not appear in NaNMTi0.3OF (Fig. 5(d2)). Moreover, upon further charging to 4.4 V, the P2–OP4 phase transition occurs, indicating the suppression of Na^+/vacancy ordering. Nie *et al.* [68]

demonstrated that K/F codoping in $K_{0.05}Na_{0.62}MnO_{1.95}F_{0.05}$ promotes the reversible lattice oxygen redox reaction. From the cyclic voltammetry (CV) test, the peak position difference near 4.2 V decreases, and the peak shape becomes more symmetric after codoping, indicating that anion redox becomes more reversible after codoping. In addition, the Na layer spacing is enlarged after codoping, lowering the Na^+ migration energy barrier. Because of the collaborative effect of K^+ and F^-, $K_{0.05}Na_{0.62}MnO_{1.95}F_{0.05}$ exhibits a good discharge capacity of 140.2 mAh·g^{-1} at 0.1 C, and the capacity retention is improved to 73% over 100 cycles.

3.2. Homogeneous surface coating

Homogeneous surface coating mainly has two functions: (1) mitigating the side reactions between the electrode and electrolyte/air and (2) improving the ionic conductivity of the cathode material. Metal oxides, phosphates, and polymers are the most common surface coating materials [69]. Here, homogeneous surface coating can be divided into two categories: (1) inorganic materials surface coating and (2) organic materials surface coating.

3.2.1. Inorganic materials surface coating

Al_2O_3, ZnO, MgO, ZrO_2, and CeO_2 are commonly used metal oxide coating layer materials whose function is to mitigate side reactions between the electrode and electrolyte [70–74]. Chang *et al*. [75] synthesized Al_2O_3-coated P2-$Na_{2/3}Fe_{1/2}Mn_{1/2}O_2$ (NFMO@Al_2O_3) using ultrasonic spray pyrolysis followed by the high-temperature solid-state method. When NFMO is exposed in the air (relative humidity of ~15%) from 15 to 30 days, the diffraction peak intensity of $Na_2CO_3·H_2O$ generated from the reaction between NFMO and $CO_2/O_2/H_2O$ increases obviously. Electrochemically insulated $Na_2CO_3·H_2O$ deteriorates the diffusion kinetics and leads to aggravated polarization. The Al_2O_3 layer successfully coated on the surface of NFMO is proved by a high-resolution transmission electron microscopy (HRTEM) image (Fig. 6(a1)). Exposed to the air under the same conditions as NFMO, NFMO@Al_2O_3 has diffraction peaks almost unchanged in position and intensity compared to the spectrum of the primary sample, indicating that it maintains the primary crystal structure (Fig. 6(a2)). The concentrations of Na_2CO_3 and $Na_2CO_3·H_2O$ on the surfaces of NFMO and NFMO@Al_2O_3 are confirmed by ICP. NFMO@Al_2O_3 stored in the air for 30 days shows a Na^+ concentration far smaller than that of NFMO, indicating that the Al_2O_3 layer effectively inhibits deterioration from the air. Under the protection from Al_2O_3, the capacity of NFM@Al_2O_3 after 40 cycles is 124.24 mAh·g^{-1}, corresponding to a capacity retention of 84.7%, higher than that of NFM (Fig. 6(a3)). Although metal oxides can prevent direct contact between electrolyte and electrode and mitigate the dissolution of a redox-active metal into the electrolyte, the poor ionic conductivity of metal oxides is unfavorable for rapid Na^+ diffusion. Shao *et al*. [76] designed a $Na_3Zr_2Si_2PO_{12}$-coated P2-$Na_{0.612}K_{0.056}MnO_2$ (NKMO@NZSP-2) using the wet chemical method. The Na^+ super ionic conductor (NASICON) $Na_3Zr_2Si_2PO_{12}$ shows a stable framework and three-dimensional Na^+ channel, boosting ionic conductivity at the electrode/electrolyte interface. As shown in Fig. 6(b1), The HRTEM image shows various lattice fringes from NKMO and NZSP, confirming that NZSP is intimately coated on the NKMO surface. Because of the erosion of HNO_3 in the synthesis process and the exchange of Na^+/K^+ with H^+, Mn^{3+} is oxidized to Mn^{4+}, which is confirmed by an XPS measurement. As shown in Fig. 6(b2), the Mn^{3+}-to-Mn^{4+} ratio is higher in NKMO than in NKMO@NZSP-2, indicating a decreased Jahn–Teller effect after coating. In addition, the diffusion coefficient is enhanced by NZSP coating, meaning that NZSP provides a faster Na^+ diffusion channel for NKMO. NKMO@NZSP-2 exhibits good electrochemical performance, with an initial capacity of 195.5 mAh·g^{-1} and a capacity retention of 71.71% after 50 cycles (Fig. 6(b3)). Moreover, NKMO@NZSP-2 shows a good low-temperature cycling performance, with a capacity retention of 76.11% after 100 cycles at −20°C.

3.2.2. Organic materials surface coating

Organic materials have also been widely used for surface coating because of their high electrical conductivity [77–78]. Lin *et al*. [79] coated PMAA–AN (copolymer nanolayer of methacrylic acid and acrylonitrile) on the $Na_{0.67}Li_{0.16}Ni_{0.33}Mn_{0.67}O_{2+\delta}$ (NLNM) surface by solution polymerization. An amorphous ultrathin organic nanolayer is evenly covered on the NLNM surface (Fig. 6(c1)). As shown in Fig. 6(c2) and (c3), compared to NLNM, 0.5wt% PMAA–AN@NLNM exhibits less potential deviation of Mn^{3+}/Mn^{4+} and a smaller peak intensity decrease in Mn^{3+}/Mn^{4+} and Ni^{2+}/Mn^{4+}, indicating that the PMAA–AN layer can enhance interfacial stability and slow voltage decay. Electrochemical impedance spectroscopy (EIS) shows that 0.5wt% PMAA–AN@NLNM has a lower charge transfer resistance, indicating that the PMAA–AN layer can improve kinetic performance. At high voltage (~4.5 V), Ni^{4+} readily forms byproducts in the electrode/electrolyte interface, while XPS shows that the Ni^{4+} content decreases with increasing coating content because of the tight lock between strongly coordinating groups of PMAA–AN and transition metal ions (Fig. 6(c4) and (c5)). The decrease in Ni^{4+} content indicates that the dissolution of active metal and side reactions are suppressed by PMAA–AN coating. As shown in Fig. 6(c6), the robust coordination induced by the strong electro-donating groups of organic PMAA–AMN ensures the better cycling performance of 0.5wt% PMAA–AN@NLNM.

3.3. Concentration gradient modification

Concentration gradient modification refers to constructing a layer with a content gradient from the outer surface to the interface/bulk, which can be divided into the full concentration gradient type and surface concentration gradient type [80]. This concentration gradient structure provides a stable outer surface and a high-capacity bulk composition. Gao *et al*. [81] synthesized concentration gradient $Na_{0.65}Ni_{0.16}Co_{0.14}Mn_{0.7}O_2$ (CG-NCM) through coprecipitation and high-temperature calcination. The composition changes the gradient

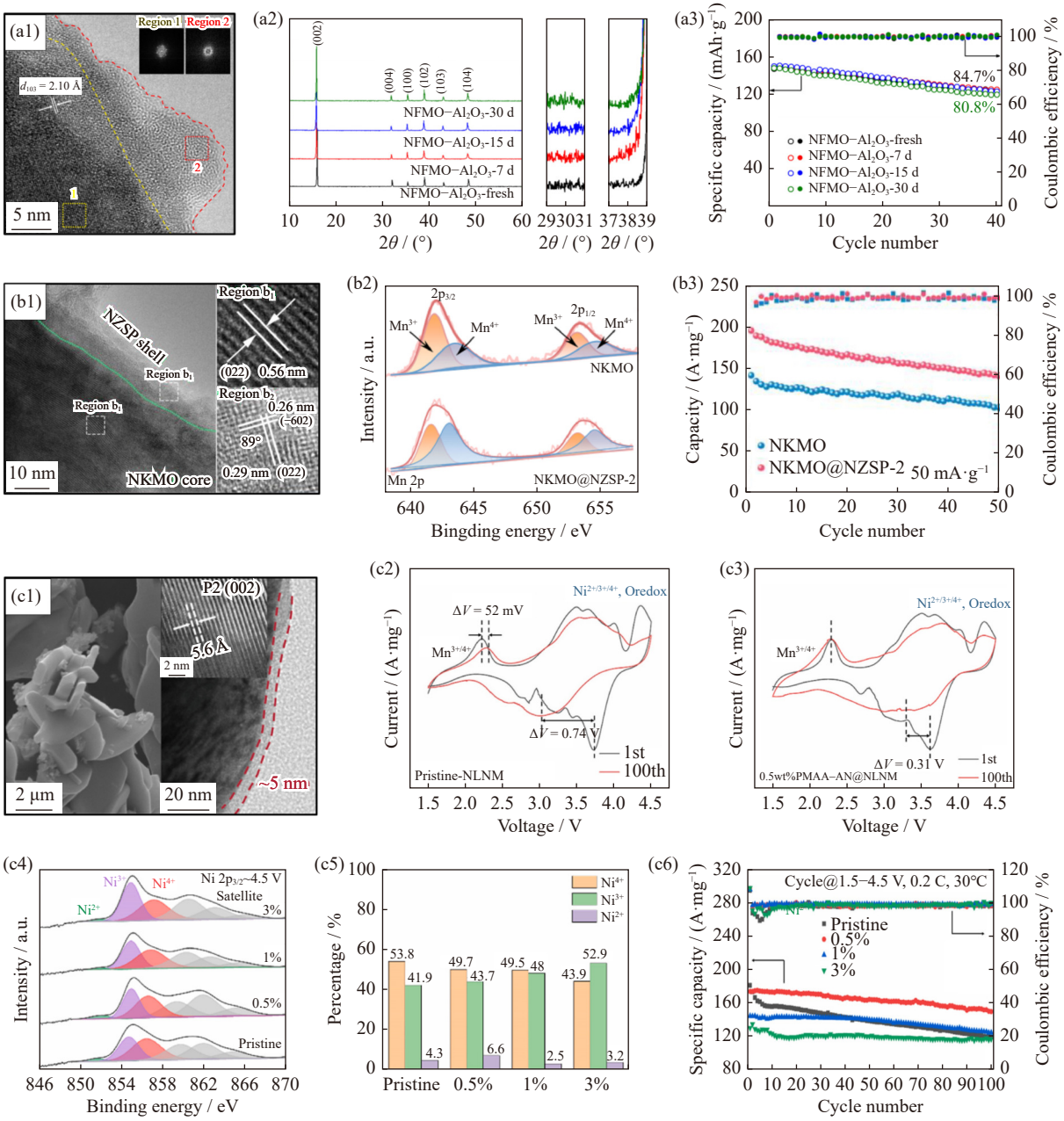

Fig. 6. (a1) HRTEM image and corresponding FFT images of Regions 1 and 2 of NFMO-Al_2O_3 samples; (a2) XRD patterns of NFMO–Al_2O_3 materials before and after storage in air; (a3) electrochemical cycling performance at 0.1 C [75]. (b1) HRTEM images of the NKMO@NZSP-2 sample in different regions; (b2) high-resolution Mn 2p XPS spectra of NKMO and NKMO@NZSP-2; (b3) cycling performances of NKMO and NKMO@NZSP-2 at 500 mA·g^{-1} [76]. (c1) scanning electron microscope (SEM) and transmission electron microscopy (TEM) images of 0.5wt% PMAA–AN@NLNM. CV curves of (c2) pristine NLNM and (c3) 0.5wt% PMAA–AN@NLNM at the 1st and 100th electrochemical cycle; (c4) Ni 2p XPS spectra of samples with different components of the organic polymer when charged at 4.5 V; (c5) distribution diagram of Ni ions with various valences when first charged to 4.5 V; (c6) capacity retention at 0.2 C of different samples [79]. (a1–a3) Reprinted from *Trans. Nonferrous Met. Soc. China*, 32, Y.J. Chang, G.H. Xie, Y.M. Zhou, *et al.*, Enhancing storage performance of P2-type $Na_{2/3}Fe_{1/2}Mn_{1/2}O_2$ cathode materials by Al_2O_3 coating, 262, Copyright 2022, with permission from Elsevier. (b1–b3) Reprint from *Electrochim. Acta*, 442, Y.Q. Shao, X.X. Wang, B.C. Li, *et al.*, Functional surface modification of P2-type layered Mn-based oxide cathode by thin layer of NASICON for sodium-ion batteries, 14915, Copyright 2023, with permission from Elsevier. (c1–c6) Reprint from *J. Power Sources*, 552, J.L. Lin, Q. Huang, K. Dai, *et al.*, Mitigating interfacial instability of high-voltage sodium layered oxide cathodes with coordinative polymeric structure, 232235, Copyright 2022, with permission from Elsevier.

from the core $Na_{0.65}Ni_{0.01}Co_{0.01}Mn_{0.98}O_2$ to shell $Na_{0.65}Ni_{0.31}Co_{0.27}Mn_{0.42}O_2$. The CG-NCM plate particles are smaller and smoother than $Na_{0.65}Ni_{0.16}Co_{0.14}Mn_{0.7}O_2$ (NCM), indicating that CG-NCM has a higher diffusion rate of Na^+ and a better tolerance of structural deformation. The EIS test shows that the contact resistance of CG-NCM is lower than that of NCM, indicating a rapid diffusion process. Hwang *et al.* [82] designed a radially aligned hierarchical columnar structure

(RAHC) in spherical with the bulk composition of $Na[Ni_{0.75}Co_{0.02}Mn_{0.23}]O_2$ and the surface composition of $Na[Ni_{0.58}Co_{0.06}Mn_{0.36}]O_2$. Atomic absorption spectroscopy shows that the average chemical composition of the product is $Na[Ni_{0.60}Co_{0.05}Mn_{0.35}]O_2$ (bulk). The element distribution of the columnar structure is confirmed by electro-probe microanalysis, with Mn and Co increasing from the bulk to the surface, while Ni decreases. RAHC delivers a capacity of 157 $mAh·g^{-1}$, higher than 145 $mAh·g^{-1}$ for the bulk. In contrast to the fast capacity fading of the bulk (capacity retention of 49.2% over 100 cycles at 0.5 C), RAHC exhibits a discharge capacity of 125.7 $mAh·g^{-1}$ after 100 cycles, corresponding to a capacity retention of 80%. In addition, the full cell embedded with RAHC and hard carbon shows excellent low-temperature performance, with a full cell capacity retention of 92% at −20°C. Bao *et al*. [83] constructed a Mn^{4+} concentration gradient spherical P2-$Na_{0.67}Ni_{0.33}Co_{0.33}Mn_{0.33}O_2$ using the coprecipitation method. The energy dispersive X-ray spectroscopy (EDS) mappings of the concentration gradient sample show that the Mn concentration is higher and the Ni concentration is lower on the surface compared to the bulk. From the CV test, P2-$Na_{0.67}Ni_{0.33}Co_{0.33}Mn_{0.33}O_2$ shows a sharp decrease in the intensity of anodic and cathodic peaks at higher voltage, while the concentrated gradient sample shows a slight decrease in these peaks. Thus, the structural stability of the concentrated gradient sample is higher than that of P2-$Na_{0.67}Ni_{0.33}Co_{0.33}Mn_{0.33}O_2$. Furthermore, compared to P2-$Na_{0.67}Ni_{0.33}Co_{0.33}Mn_{0.33}O_2$, the Mn-rich surface in the concentration gradient sample can mitigate Ni dissolution, contributing to better cycling stability, with a capacity retention of 84.5% over 100 cycles at 100 $mA·g^{-1}$. Guo *et al*. [84] synthesized $NaMnTi_{0.1}Ni_{0.1}O_2$ (NMTN) with a Ti-rich surface and a Mn-rich layered bulk ($NaMn_{0.8}Ti_{0.1}Ni_{0.1}O_2$) by solid-state reaction. The chemical composition was scanned by elemental-resolution electron energy-loss spectroscopy (EELS), as shown in Fig. 7(a1)–(a4). The Ti content increases from the bulk to the surface with a two-fold difference; Na, Mn, and Ni are homogeneously dispersed in the bulk; and the contents of Na and Mn decrease in the range of 7.33–9.42 nm (the yellow-dash region). This surface recon-

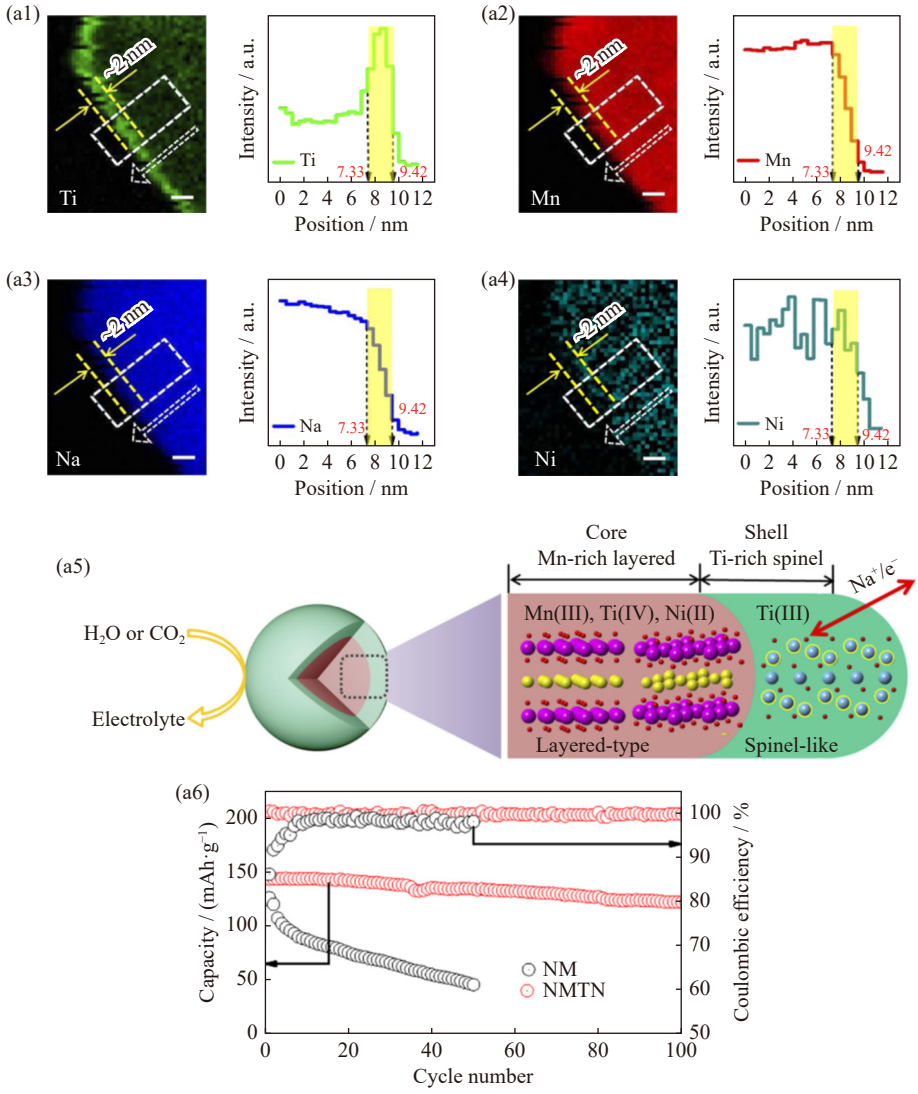

Fig. 7. (a1–a4) EELS chemical mapping of the NMTN samples and the corresponding chemical compositions (white rectangle) for Ti, Na, Mn, and Ni; (a5) 3D structural model of the NMTN samples composed of a Ti-rich spinel-like interface (green shell) and Mn-rich layered bulk (brown core); (a6) cycling performance of the NMTN electrode at a rate of 0.5 C [84].

struction builds a structure with a Mn-rich layered core and a Ti-rich spinel shell, as shown in Fig. 7(a5). The Ti-rich spinel shell effectively inhibits the side reaction between the electrode and air/electrolyte. The electron conductivity, ionic conductivity, and structural stability are enhanced by this overlayer. Therefore, NMTN exhibits good electrochemical performance. The discharge capacity of NMTN is 186 mAh·g^{-1}, and the capacity retention of NMTN over 100 cycles is 85% (Fig. 7(a6)).

3.4. Designing the mixed structure

The P2-type structure has an open prismatic diffusion pathway that ensures a good rate performance, but the high operating voltage causes electrolyte decomposition and structural degradation. The O3-type structure has a high Na content that ensures higher capacity, but the easy reaction between the electrode and H_2O/CO_2 in the air dramatically deteriorates electrochemical performance. To use the synergistic effect between the P2 and O3 structures, designing a hybrid phase has been considered an effective method for exploring long-cycle life cathode material, in which the composition of the hybrid phase can be regulated by the synthesis conditions and element content [85]. Xiao *et al*. [86] explored a series of P2/O3 hybrid cathode materials according to the phase diagram of $Na_xMn_yNi_{1-y}O_2$, as shown in Fig. 8(a1). The capacity retentions of Na0.85NMT, Na0.85NMC,

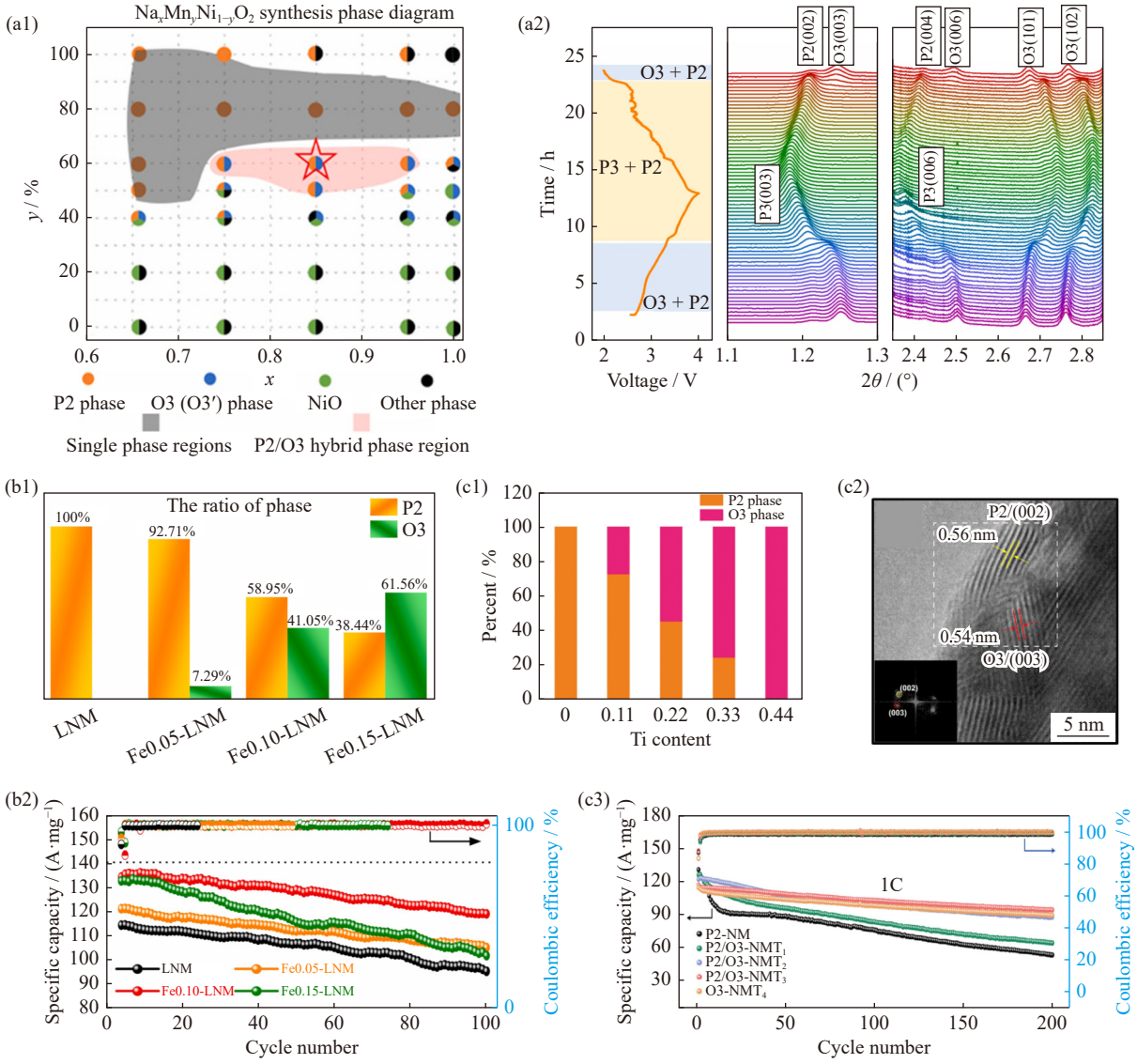

Fig. 8. (a1) Synthesis phase diagram of $Na_xMn_yNi_{1-y}O_2$ at a sintering temperature of 900°C; (a2) *in-situ* XRD pattern of P2/O3-Na0.85NMF [86]. (b1) phase ratio for P2 and O3 at different Fe contents; (b2) cycling performances of different samples at 1 C [87]. (c1) schematic of phase proportions at different Ti contents; (c2) HRTEM image of NMT3; (c3) cycling performances of NM, NMT1, NMT2, NMT3, and NMT4 [88]. (a1, a2) Reprint from *Nano Energy*, 89, B.W. Xiao, X. Liu, M. Song, *et al*., A general strategy for batch development of high-performance and cost-effective sodium layered cathodes, 106371, Copyright 2021, with permission from Elsevier. (b1, b2) Reprint from *J. Power Sources*, 553, J.M. Feng, D. Fang, Z. Yang, *et al*., A novel P2/O3 composite cathode toward synergistic electrochemical optimization for sodium ion batteries, 232292, Copyright 2022, with permission from Elsevier. (c1–c3) Reprint from *Energy Storage Mater*., 50, L.Z. Yu, Z.W. Cheng, K. Xu, *et al*., Interlocking biphasic chemistry for high-voltage P2/O3 sodium layered oxide cathode, 730, Copyright 2022, with permission from Elsevier.

Na0.85NMF, and NaNMF after 500 cycles are 91%, 90.6%, 86.2%, and 80.6%, respectively. The *in-situ* XRD of P2/O3-Na0.85NMF is used to understand the structural stability of the P2/O3 phase. In the yellow region shown in Fig. 8(a2), the diffraction peaks of the P2 structure overlap with those of the P3 structure, and the presence of the P2 structure increases the energy required for layer gliding. During discharging, diffraction peaks of the P2 phase reappear. It is likely that the P2 phase exists throughout the charge/discharge process, leading to the high stability of Na0.85NMF. Feng *et al*. [87] synthesized a series of P2/O3-$Na_{0.80}Li_{0.13}Ni_{0.20}Fe_xMn_{0.67-x}O_2$ (Fe*x*-LNM) by regulating iron content through a high-temperature solid-state method. The proportion of O3 increases with the iron content, as shown in Fig. 8(b1). A distinct phase boundary between P3 and O3 can be observed using HRTEM. Compared to P2-LNM, Fe0.10-LNM not only has a higher discharge capacity of approximately 172.02 $mAh·g^{-1}$ and a higher initial coulombic efficiency of approximately 85.39% but also maintains a good capacity retention of 88.6% over 100 cycles (Fig. 8(b2)). Yu *et al*. [88] prepared P2/O3-$Na_{0.85}Ni_{0.34}Mn_{0.66-x}Ti_xO_2$ (NMT_x) by tuning the Ti^{4+} content. With increasing Ti^{4+} content, the proportion of the O3 structure increases Fig. 8(c1). In Fig. 8(c2), the HRTEM image shows different planar distances. The planar distance of 0.56 nm corresponds to the (002) crystal face of the P2 structure, and the planar distance of 0.54 nm corresponds to the (003) crystal face of the O3 phase. NMT3 exhibits a higher specific capacity of 94.1 $mAh·g^{-1}$ after 200 cycles at 1 C, corresponding to a capacity retention of 80.6% (Fig. 8(c3)). This good cycling performance is due to the prevention of ordered Na^+/vacancies and increased structural stability after introducing Ti^{4+}.

3.5. Particle engineering

Particle engineering includes single-crystal construction, active facet construction, and morphological manipulation. Single crystals show less particle cracking and surface area, which helps achieve better air stability and cycling performance. Darga and Manthiram [89] prepared single-crystal $NaNi_{0.5}Mn_{0.5}O_2$ (MS-SNMO) particles using sodium chloride and metal oxides as raw materials by the two-step molten salt method. For comparison, the author prepared polycrystalline $NaNi_{0.5}Mn_{0.5}O_2$ (PC-SNMO). After 200 cycles, MS-SNMO and PC-SNMO maintain 69% and 35% capacity retention, respectively. As shown in Fig. 9(a1) and (a2), because of volume expansion, PC-SNMO particles crack severely along the boundary as primary particles push against each other. MS-SNMO particles show less cracking because fewer particles push against each other during the volume expansion process (Fig. 9(a3) and (a4)). Cracking results in more surfaces being exposed to electrolytes, exacerbating capacity degradation. As shown in Fig. 9(a5), MS-SNMO exhibits a capacity retention of 69% after 200 cycles, higher than 35% for PC-SNMO. Lamb *et al*. [90] synthesized two O3-type $Na(Ni_{0.3}Fe_{0.4}Mn_{0.3})O_2$ single crystals using hydroxide and oxide as raw materials by the molten salt method and prepared a control sample by the solid-state method. The capacity retention of the control, hydroxide, and oxide samples over 100 cycles is 61%, 67%, and 76%, respectively (Fig. 9(b1)). The control sample shows a spherical secondary particle morphology, and molten salt-synthesized samples show a microsized platelet-like morphology with a narrow width. This narrow width of the single-crystal sample reduces the side reactions occurring along the edge planes, indicating less total surface degradation. Moreover, the single-crystal sample shows less capacity loss when exposed to 50% humidity air for two weeks, as shown in Fig. 9(b2), further proving that a smaller exposed edge plane benefits ambient stability. The active facet construction has been adopted to improve electrochemical performance because of its faster diffusion kinetics [91]. Xiao *et al*. [92] designed $Na[Li_{0.05}Ni_{0.3}Mn_{0.5}Cu_{0.1}Mg_{0.05}]O_2$ with exposed {010} active facets using the thermal polymerization method followed by the high-temperature method. Compared to the 205.8 nm thickness of {010} in O3-$NaNi_{0.5}Mn_{0.5}O_2$, $Na[Li_{0.05}Ni_{0.3}Mn_{0.5}Cu_{0.1}Mg_{0.05}]O_2$ exhibits a thickness of {010} of approximately 384.7 nm, providing more Na^+ diffusion channels. $Na[Li_{0.05}Ni_{0.3}Mn_{0.5}Cu_{0.1}Mg_{0.05}]O_2$ shows 91.9% capacity retention over 600 cycles and maintains a stable coulombic efficiency. Zhang *et al*. [93] synthesized hexagonal-prism-like single-crystal P2-$Na_{0.66}Ni_{0.26}Zn_{0.07}Mn_{0.67}O_2$ with a high proportion of {001} planes through coprecipitation followed by the molten salt method (denoted as MC-NNZM). For comparison, the author synthesized the same composition by the traditional solid-state method (denoted as S-NNZM). As shown in Fig. 9(c1) and (c2), above 3.8 V, the intensity of the oxidation peaks of MC-NNZM is lower than that of S-NNZM because of the suppression of the P2–OP4 phase transition and side reactions. The reduction peaks of MC-NNZM overlap well with the first three cycles and are sharper than those of S-NNZM, indicating better intercalation kinetics in MC-NNZM. MC-NNZM exhibits a capacity retention of 95.8% over 100 cycles, higher than 79.8% for S-NNZM (Fig. 9(c3)). The SEM images of S-NNZM and MC-NNZM after 50 cycles are shown in Fig. 9(c4) and (c5), S-NNZM shows more delamination cracks and dislocations, while MC-NNZM shows only fewer gliding lines. Moreover, MC-NNZM shows a smaller increase in peak intensity associated with the Na–F, C–O, C=O, and O–C=O bonds after 10 cycles (Fig. 9(c6)–(c9)), indicating that the interfacial stability has been improved by optimizing the crystal orientation of the single-crystal structure.

Apart from the construction of single-crystal and active facets, morphological manipulation is a useful method for improving the cycling performance of layered oxide cathode materials. Spherical particles with uniform size distribution can substantially improve the tap density and produce better electrodes because of their excellent flowability and dispersibility [94–95]. Wang *et al*. [96] compared the electrochemical performances of spherical $NaCrO_2$ (s-$NaCrO_2$) and irregular $NaCrO_2$ (i-$NaCrO_2$) (Fig. 10(a1) and (a2)). s-$NaCrO_2$ synthesized using the hydrothermal method has an initial dis-

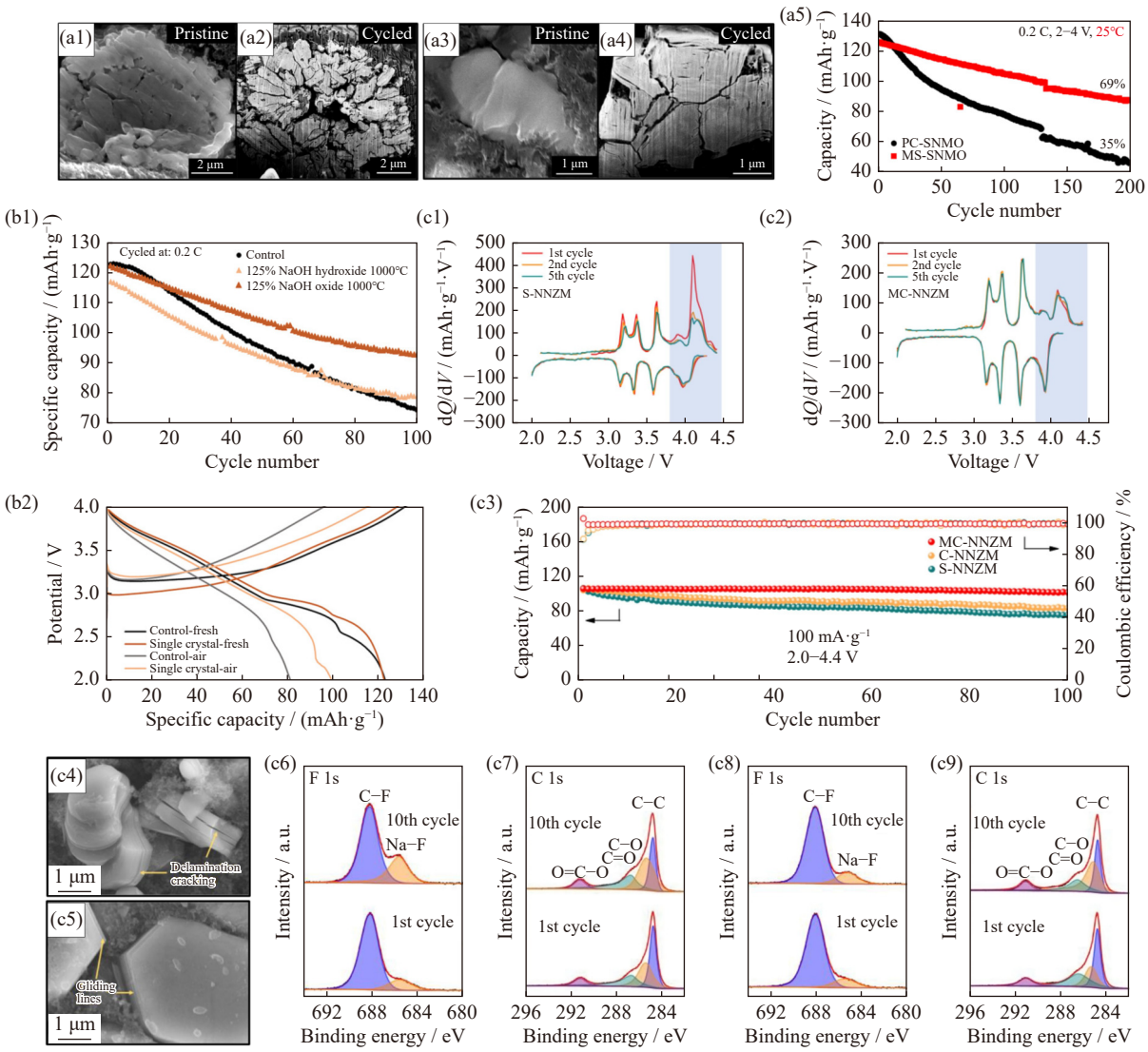

Fig. 9. Cross-sectional SEM image of (a1) pristine polycrystalline particles (PC-SNMO) dispersed in carbon/PVdF and (a2) a FIB-SEM image of PC-SNMO particles after 200 cycles; (a3) cross-sectional SEM image of a pristine MS-SNMO particle and (a4) a FIB-SEM image of MS-SNMO particles after 200 cycles; (a5) cycling performances of PC-SNMO and MS-SNMO [89]. (b1) cycle life and (b2) first cycle charge–discharge curves of the control and coprecipitated material compared to molten salt-synthesized samples made with 125% NaOH at 1000°C from the coprecipitated hydroxide precursor or ground metal oxides [90]. dQ/dV plots of (c1) S-NNZM and (c2) MC-NNZM at 10 mA·g^{-1}; (c3) cycling performances of S-NNZM and MC-NNZM. SEM images of (c4) S-NNZM and (c5) MC-NNZM. F 1s and C 1s XPS spectra of (c6, c7) S-NNZM and (c8, c9) MC-NNZM after 1 and 10 cycles [93]. (a1–a5) Reprint with permission from J. Darga, and A. Manthiram, *ACS Appl. Mater. Interfaces*, 14, 52729–52737 (2022) [89]. Copyright 2022 American Chemical Society. (b1, b2) J. Lamb, K. Jarvis, and A. Manthiram, *Small*, 18, 2106927 (2022) [90]. Copyright 2022 Wiley-VCH Verlag GmbH & KGaA. Reproduced with permission. (c1–c9) Reprint from *Chem. Eng. J.*, 458, F.P. Zhang, Y. Lu, Y. Guo, *et al.*, Highly stabilized single-crystal P2-type layered oxides obtained via rational crystal orientation modulation for sodium-ion batteries, 141515, Copyright 2023, with permission from Elsevier.

charge capacity of 118 mAh·g^{-1} at 0.2 C, higher than that of i-$NaCrO_2$ synthesized using the solid-state method. Because of the high structural strength of its submicrospheres, s-$NaCrO_2$ delivers a capacity of 98 mAh·g^{-1} after 800 cycles, with a capacity retention of 90%, higher than 61% for i-$NaCrO_2$ (Fig. 10(a3)). After 1500 cycles at 20 C, s-$NaCrO_2$ still retains high crystallinity, as shown in Fig. 10(a4). In addition to the spherical morphology, particles with morphologies, such as nanofiber, nanowires, and nanorods, also show excellent cycling performance [97–98]. Kalluri *et al.* [99] synthesized $Na_{2/3}(Fe_{1/2}Mn_{1/2})O_2$ nanofibers (NFMO NF) by electrospinning, as shown in Fig. 10(b1). This material shows an initial discharge capacity of 195 mAh·g^{-1} at 0.1 C, higher than 179 mAh·g^{-1} for $Na_{2/3}(Fe_{1/2}Mn_{1/2})O_2$ nanoparticles (NFMO NP, Fig. 10(b2)) prepared using the sol-gel method (Fig. 10(b3)). The capacity retention of NFMO NF after 80 cycles at 0.1 C is 86.4%, higher than 60% for NFMO NP, as shown in Fig. 10(b4). Aragón *et al.* [100] reported P2-$Na_{2/3}Fe_{1/3}Mn_{2/3}O_2$ nanorods and nanoplates using the emulsion-based method (Fig. 10(c1) and (c2)). Compared to $Na_{2/3}Fe_{1/3}Mn_{2/3}O_2$ microparticles by the sol-gel method, nanorods and nanoplates have a higher capacity retention (Fig. 10(c3)). This result is due to the nanometric morphology, which helps reduce the effect of structural transformation on reversibility. In addi-

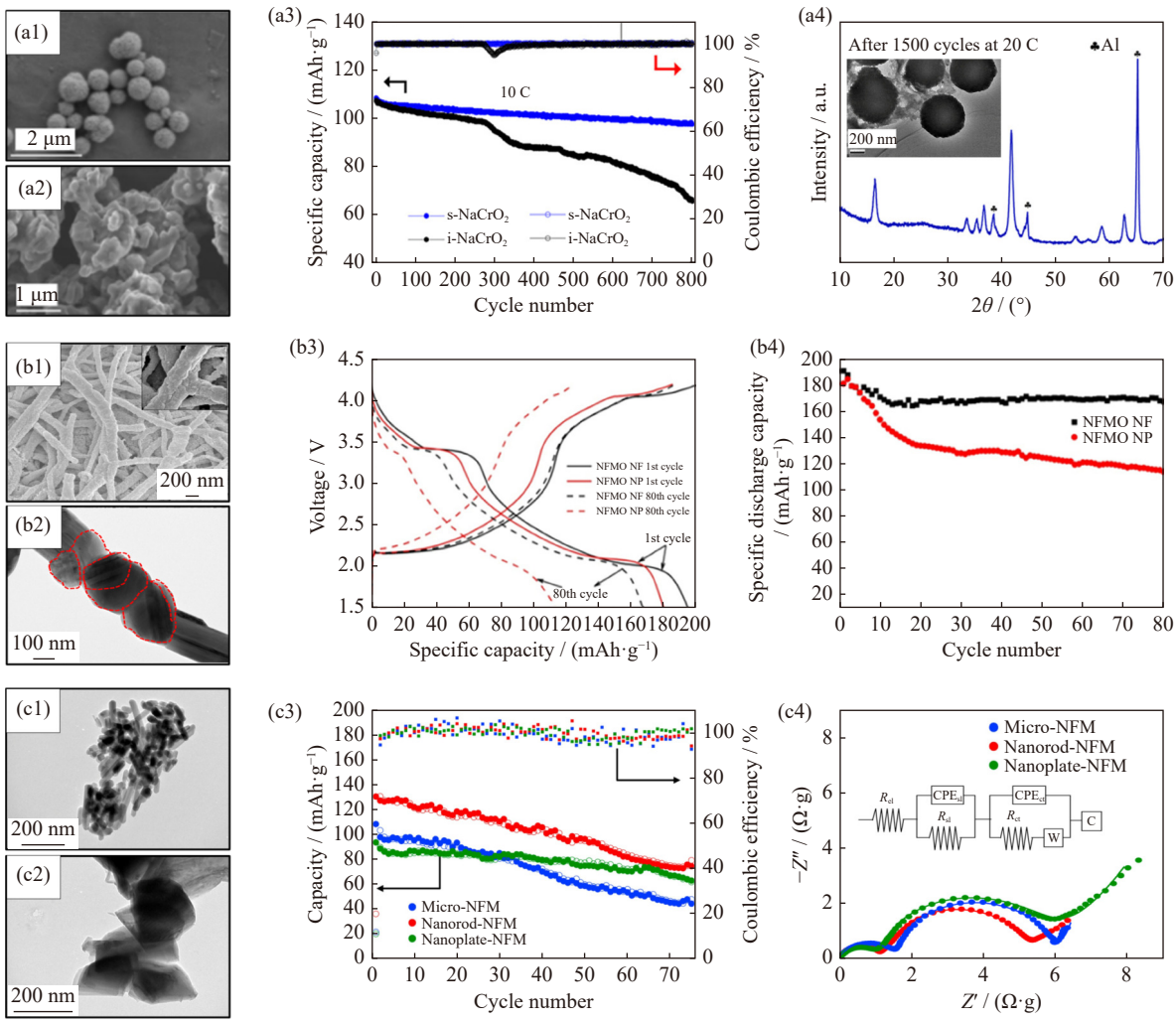

Fig. 10. SEM images of (a1) s-$NaCrO_2$ and (a2) i-$NaCrO_2$; (a3) cycling performances of s-$NaCrO_2$ and i-$NaCrO_2$; (a4) XRD pattern and TEM image of i-$NaCrO_2$ after 1500 cycles [96]. SEM images of (b1) NFMO NF and (b2) NFMO NP. (b3) charge–discharge curves of NFMO NF and NFMO NP at 0.1 C. (b4) cycling performances of NFMO NF and NFMO NP [99]. TEM of (c1) nanorod-NFM and (c2) nanoplate-NFM; (c3) cycling performances of micro-NFM, nanorod-NFM, and nanoplate-NFM; (c4) Nyquist plots of NFM samples recorded after the first cycle at 0.05 C (R_{ct} and R_{sl} refer to the charge-transfer resistances at the interphase and the internal resistances at the surface layer, respectively. R_{el} refers to the ohmic drop at the electrolyte. CPE_{ct} and CPE_{sl} refers to constant phase element. W refers to Warburg element. C refers to Capacitance.) [100]. (a1–a4) Reprint with permission from S. Wang, F. Chen, X.D. He, *et al.*, *ACS Appl. Mater. Interfaces*, 13, 12203–12210 (2021) [96]. Copyright 2021 American Chemical Society. (b1–b4) Reprint with permission from S. Kalluri, K.H. Seng, W.K. Pang, *et al.*, *ACS Appl. Mater. Interfaces*, 6, 8953–8958 (2014) [99]. Copyright 2014 American Chemical Society. (c1–c4) Reprint from *J. Alloys Compd.*, 724, M.J. Aragón, P. Lavela, G. Ortiz, R. Alcántara, and J.L. Tirado, Nanometric P2-$Na_{2/3}Fe_{1/3}Mn_{2/3}O_2$ with controlled morphology as cathode for sodium-ion batteries, 465, Copyright 2017, with permission from Elsevier.

tion, the nanorods show lower R_{ct} (charge-transfer resistance) values (Fig. 10(c4)), illustrating that the activation barriers imposed on Na^+ migration by the interphase boundary are reduced.

3.6. Designing high-entropy material

Recently, high-entropy layered oxides have been widely studied because of the entropy-dominated phase stabilization effects [101–103]. High-entropy refers to a multi-component system with at least five elements in one Wyckoff position. Murty, Yeh, and Ranganathan [104] introduced the classification of "high-entropy" for materials with molar configurational entropy (S_{config}) above 1.5R. According to the Gibbs–Helmholtz equation, $\Delta G_{mix} = \Delta H_{mix} - T\Delta S_{mix}$, where ΔG_{mix} is mixing free energy, ΔH_{mix} is mixing enthalpy, and ΔS_{mix} is mixing entropy. When $S_{config} \geq 1.5R$, $T\Delta S_{mix}$ is large enough to overcome ΔH_{mix} and dominate the free energy, indicating that high temperatures favor the formation of high-entropy materials [105]. Anand *et al.* [106] demonstrated entropy-dominated phase stabilization effects through molecular dynamics simulations. ΔH_{mix} and ΔS_{mix} work synergistically for a stable system ($\Delta G_{mix} < 0$). ΔH_{mix} and ΔS_{mix} increase with the types of cations, and ΔS_{mix} dominates ΔG_{mix} when the number of types of cations is 4 and 5. In other words, $T\Delta S_{mix}$ is large enough in high-entropy material to make ΔG_{mix} negative.

One type of high-entropy, layered oxide, is composed of different cations in equal proportions. Walczak *et al.* [107]

reported $NaMn_{0.2}Fe_{0.2}Co_{0.2}Ni_{0.2}Ti_{0.2}O_2$ high-entropy layered oxide, finding that the multi-redox reactions of Mn, Fe, Co, and Ni contribute to a high average discharge capacity of 180 $mAh \cdot g^{-1}$ at 0.1 C. The as-prepared sample comprises O3(1) and O3(2) phases, as detected at the beginning of the first charging (Fig. 11(a1)). After deintercalation of approximately 0.05 mol Na, the rhombohedral P3 phase can be detected. Meanwhile, the two O3 phases start to disappear. The O3(1) phase is not detected until the charge voltage reaches 3.26 V, indicating that the phase transition of O3–P3 is partially reversible as shown in Fig. 11(a2). As shown in Fig. 11(a3), the capacity fades dramatically in the first 10 cycles because of the activation processes at the electrode/electrolyte interface. Surprisingly, the capacity decay from 10 cycles to 100 cycles is only 0.3%, indicating the excellent electrochemical stability of $NaMn_{0.2}Fe_{0.2}Co_{0.2}Ni_{0.2}Ti_{0.2}O_2$. In addition to the high-entropy layered oxide comprising equal proportions, high-entropy material comprising varying proportions has also been reported. Zhou *et al.* [108] synthesized $Na_{0.7}Mn_{0.4}Ni_{0.3}Cu_{0.1}Fe_{0.1}Ti_{0.1}O_{1.95}F_{0.1}$ high-entropy layered oxide using the high-temperature solid-state method. It delivers excellent capacity retention over a wide temperature range of −40 to 50°C, as shown in Fig. 11(b1), the capacity retention after 200 cycles at −40°C is 99.5% in particular. For the

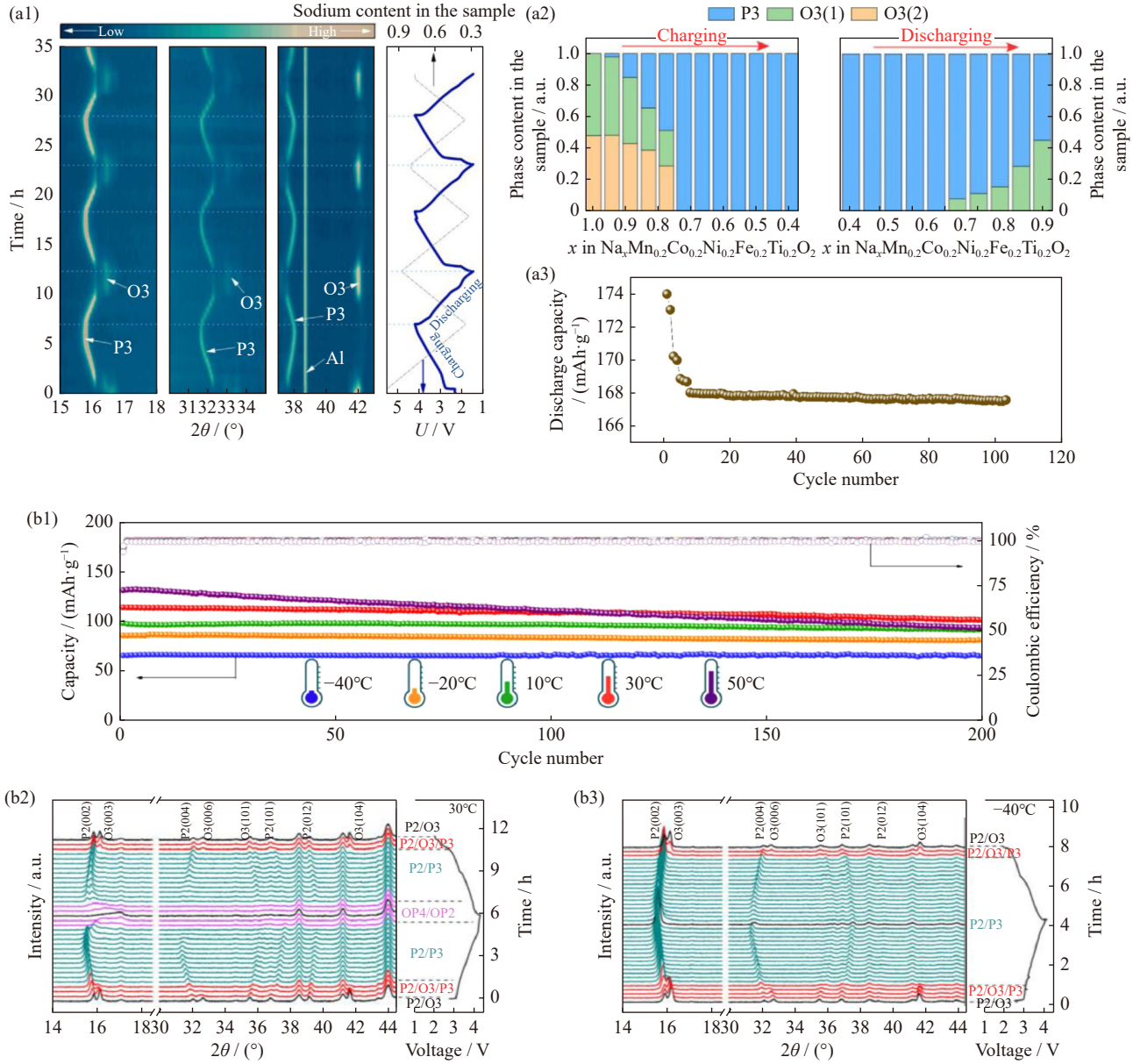

Fig. 11. (a1) Galvanostatic tests of the $Na|Na^+|Na_xMn_{0.2}Fe_{0.2}Co_{0.2}Ni_{0.2}Ti_{0.2}O_2$ cell: charge/discharge curves under various current loads in the range of 1.5–4.2 V; (a2) discharge capacity as a function of cycle number; (a3) long-term cycling for the $Na|Na^+|NaMn_{0.2}Fe_{0.2}Co_{0.2}Ni_{0.2}Ti_{0.2}O_2$ cell under a C/10 current rate [107]. (b1) cycling performances of P2/O3-NaMnNiCuFeTiOF at different temperatures. *in-situ* XRD patterns during the initial charge/discharge process at (b2) 30°C and (b3) −40°C [108]. (a1–a3) Reprint from *Energy Storage Mater.*, 47, K. Walczak, A. Plewa, C. Ghica, *et al.*, $NaMn_{0.2}Fe_{0.2}Co_{0.2}Ni_{0.2}Ti_{0.2}O_2$ high-entropy layered oxide–experimental and theoretical evidence of high electrochemical performance in sodium batteries, 500, Copyright 2022, with permission from Elsevier. (b1–b3) Reprint from *Energy Storage Mater.*, 57, P.F. Zhou, Z.N. Che, J. Liu, *et al.*, High-entropy P2/O3 biphasic cathode materials for wide-temperature rechargeable sodium-ion batteries, 618, Copyright 2023, with permission from Elsevier.

phase evolution at 30°C shown in Fig. 11(b2) and (b3), the O3–P3 phase transformation is detected at the beginning of charging, and the O3 phase completely transforms into the P3 phase when the charge voltage is 3.31 V. In the voltage range of 3.31–4.13 V, the solid solution reaction comprising P2 and P3 is detected. On further charging to 4.3 V, P2 transforms into the OP4 phase, and P3 transforms into the OP2 phase. During the subsequent discharging process, all diffraction peaks return to the pristine position, indicating that the phase transformation is reversible. This phase transformation is also observed at −40°C. When exposed to the air for 90 days, this material also maintains good reversible capacity and cycling performance. These above tests prove that high-entropy layered oxides have remarkable storage stability.

3.7. Integrated modification

To exploit the synergistic effect of different strategies, many integrated modification methods have been investigated, such as bulk doping-integrated surface coating, bulk doping-integrated concentration gradient modification, and bulk doping-integrated particle engineering [109–110]. Bulk doping-integrated surface modification is the most widely used integrated method and has two main functions: (1) improving bulk structural stability; (2) inhibiting side reactions and improving moisture stability [111]. Zhao *et al*. [112] reported $NaTi_2(PO_4)_3$-coated O3-$NaNi_{1/3}Fe_{1/3}Mn_{1/3}O_2$ (NFM@NTP), where partial Ti^{4+} ions were introduced into the bulk phase accompanied by coating. TEM and HRTEM images show a different lattice fringe between the bulk and surface, indicating that NTP successfully adheres to the NFM surface (Fig. 12(a1) and (a2)). In the cathode–electrolyte interface analysis conducted using the XPS spectra shown in Fig. 12(a3), the OH^- signal peak at 531.0 eV, resulting from the reaction between the electrolyte and the electrode surface, is detected in NFM. In contrast, fluoride in NFM@NTP has no OH^- signal and lower peak intensity, suggesting that the NTP coating layer inhibits the highly corrosive hydrofluoric acid attacks that cause electrolyte decomposition and the subsequent dissolved detrimental substance. Moreover, the introduction of Ti^{4+} induces a larger interlay spacing, indicating better structural stability. Thus, NFM@NTP shows a higher discharge capacity of 164.1 mAh·g^{-1} and a better capacity retention of 77.5% at 1 C over 100 cycles. Wang *et al*. [113] constructed multi-coating layers and bulk doping using a one-step method, as shown in Fig. 12(b1). Driven by a high-temperature process, Al^{3+} can be introduced into the

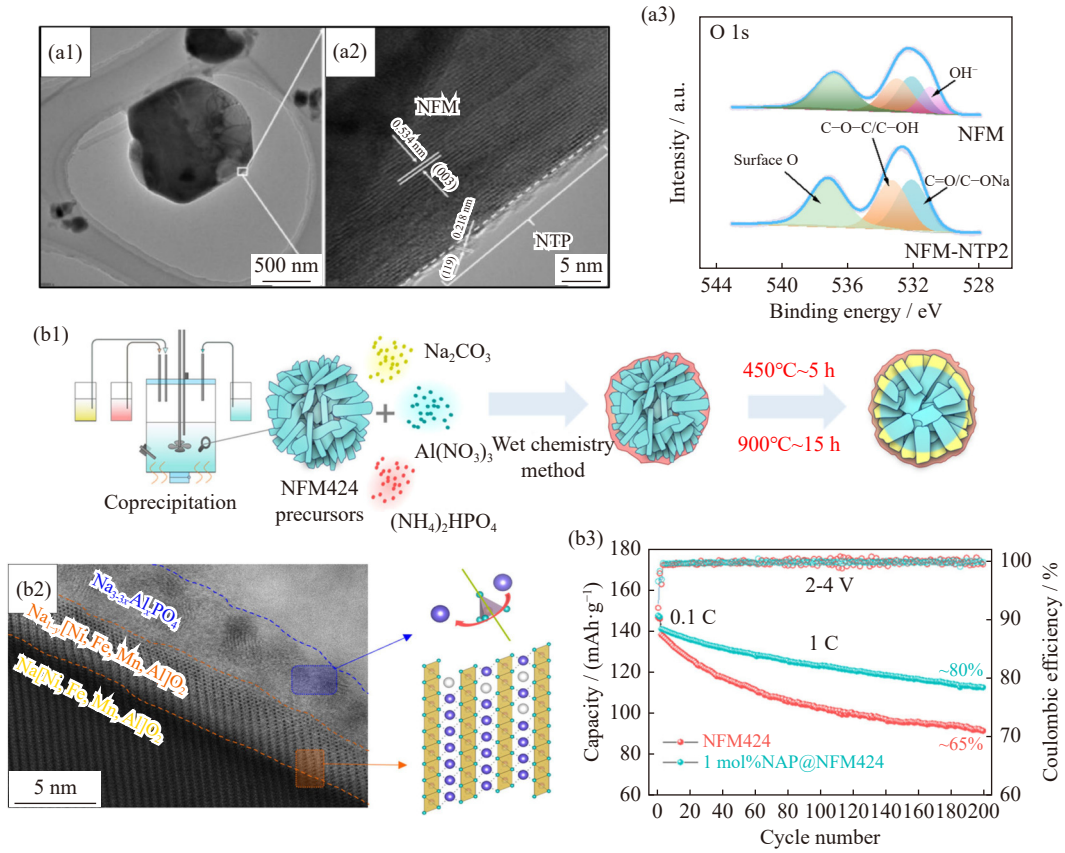

Fig. 12. (a1) TEM and (a2) HRTEM images of NFM-NTM2; (a3) XPS spectra of O elements for the NFM and NFM-NTP electrodes after cycling. (b1) Schematics of the surface coating and doping for NFM424; (b2) STEM image of a particle cross-section of modified $Na_{3(1-x)}Al_xPO_4$; (b3) cycling performance during 200 cycles at 1 C after the initial two cycles of activation at 0.1 C in the voltage range of 2.0–4.0 V [113]. (a1–a3) Reprint from *Electrochim. Acta*, 441, S.Y. Zhao, Q.H. Shi, R.J. Qi, *et al.*, $NaTi_2(PO_4)_3$ modified O3-type $NaNi_{1/3}Fe_{1/3}Mn_{1/3}O_2$ as high rate and air stable cathode for sodium-ion batteries, 141859, Copyright 2023, with permission from Elsevier. (b1–b3) Reprint with permission from H.B. Wang, F.X. Ding, Y.Q. Wang, *et al.*, *ACS Energy Lett.*, 8, 1434–1444 (2023) [113]. Copyright 2023 American Chemical Society.

bulk phase to build a robust bulk structure. $Na_{3(1-x)}Al_xPO_4$ (NAP) and $NaNi_{0.4}Fe_{0.2}Mn_{0.4}O_2$ (NFM424) compete for sodium sources in the synthesis process, resulting in three compositions from surface to bulk. As shown in Fig. 12(b2), the surface composition is NAP, the intermediate Na vacancy phase is Na_{1-y}[Ni,Fe,Mn,Al]O_2, and the bulk phase is NFM424. NFM424@NAP shows a higher initial coulombic efficiency due to less surface residual alkali, fewer side reactions, and sodium vacancies provided by Na_{1-y}[Ni,Fe,Mn,Al]O_2. As shown in Fig. 12(b3), the capacity retention of NFM424@NAP over 200 cycles can be substantially improved to 80% over the 65% capacity retention of NFM424.

4. Summary and outlook

4.1. Summary

This review focuses on the cycling performance of layered oxide materials, the causes of cycling performance deterioration, and strategies for obtaining better cycling performance, which are discussed in detail. First, a phase transition may lead to an irreversible phase change that causes the capacity to decrease, and the volume change originating from this phase transition accelerates crack formation. Second, the reaction between active materials and CO_2/H_2O accelerates structural collapse. The detrimental substance generated by the side reactions between active materials and electrolytes deteriorates the electrochemical performance. Third, the irreversible anionic oxygen reaction induces oxygen loss and then leads to severe capacity fading. Thus, layered oxide materials suffer from the challenges of phase transitions, ambient stability, side reactions, and irreversible anionic oxygen activity. Accordingly, seven strategies have been considered. To illustrate why these strategies can improve cycling performance, layered cathode materials modified by different strategies are summarized in Table 1. From the comparison and generalization in Table 1, the functions of the different

Table 1. Summary of layered cathode materials by different modification strategies

Method	Cathode material	Strategy details	Synthesis method	Electrolyte	Discharge capacity	Cycling performance	Function	Ref.
Bulk doping	P2-$Na_{0.67}Fe_{0.5}Mn_{0.5}B_{0.04}O_2$	B^{3+} doping at interstitial sites	Solid-phase reaction	1.0 mol·L^{-1} $NaClO_4$ in EC/DEC (EC:DEC = 1:1 in volume)	152 mAh·g^{-1} (0.1 C, 1.5–4.0 V)	88.8% (100 cycles, 1 C, 1.5–4.0 V)	Stabilizing transition metal layers, suppressing metal dissolution, and mitigating the Jahn–Teller effect	[30]
	P2-$Na_{0.67}Co_{0.20}Mn_{0.79}Ce_{0.01}O_2$	Ce^{3+} doping at Mn sites	Solid-state method	1.0 mol·L^{-1} $NaClO_4$ in PC/FEC (PC:FEC = 97:3 in volume)	135.8 mAh·g^{-1} (0.1 C, 1.5–4.0 V)	91.7% (400 cycles, 1 C, 2.0–4.0 V)	Improving structural stability and mitigating the Jahn–Teller effect	[31]
	O3-$NaNi_{0.328}Mn_{1/3}Fe_{1/3}Zn_{0.005}O_2$	Zn^{2+} doping at Ni sites	Solid-state method	1.0 mol·L^{-1} $NaClO_4$ in EC:DEC (EC:DEC = 1:1 in volume)	129.2 mAh·g^{-1} (0.1 C, 2.0–4.0 V)	86.53% (200 cycles, 1 C, 2.0–4.0 V)	Improving structural stability and phase transition reversibility	[32]
	O3-$Na_{0.72}Cr_{0.86}Sb_{0.14}O_2$	Sb^{5+} doping at Cr sites	Solid-state method	0.5 mol·L^{-1} $NaPF_6$ in PC/FEC (PC:FEC = 97:3 in volume)	174.69 mAh·g^{-1} (0.05 C, 1.5–4.1 V)	78.64% (200 cycles, 2 C, 1.5–4.1 V)	Suppressing Cr migration to the Na layer	[37]
	P2-$Na_{0.67}Mn_{0.65}Ni_{0.2}Mg_{0.15}O_2$	Mg^{2+} doping at Co sites	Coprecipitation method	1.0 mol·L^{-1} $NaClO_4$ in PC/FEC (PC with 2vol% FEC)	104.9 mAh·g^{-1} (0.1 C, 2.0–4.3 V)	94% (100 cycles, 0.1 C, 2–4.3 V)	Suppressing interfacial side reactions	[38]
	P2-$Na_{0.612}K_{0.056}MnO_2$	K^+ doping at Na sites	Solid-state method	1.0 mol·L^{-1} $NaPF_6$ in PC/FEC (PC containing 5wt% FEC)	240.5 mAh·g^{-1} (20 mA·g^{-1}, 1.8–4.3 V)	98.2% (100 cycles, 50 mA·g^{-1}, 1.8–4.3 V)	Reducing the phase transition and enhancing oxygen redox reversibility	[45]
	P2-$Na_{0.7}Li_{0.03}$[$Mg_{0.15}Li_{0.07}Mn_{0.75}$]$O_2$	Li^+ doping at Na and Mn sites	Solid-state method	1.0 mol·L^{-1} $NaPF_6$ in PC/FEC (PC with 2wt% FEC)	266 mAh·g^{-1} (0.05 C, 1.5–4.6 V)	80.9% (50 cycles, 0.5 C, 1.8–4.6 V)	Suppressing the phase transition	[13]
	O3-$NaNi_{1/3}Fe_{1/3}Mn_{1/3}O_{1.95}F_{0.05}$	F^- doping at O sites	Coprecipitation method	1.0 mol·L^{-1} $NaClO_4$ in PC/FEC (PC with 5wt% FEC)	144.9 mAh·g^{-1} (0.5 C, 2.0–4.0 V)	84% (100 cycles, 2 C, 2.0–4.0 V)	Mitigating the Jahn–Teller effect and inhibiting the slip of the interlayer	[50]
	P2-$Na_{2/3}Ni_{1/3}Mn_{2/3}O_{1.95}F_{0.05}$	F^- doping at O sites	Solid-state method	1.0 mol·L^{-1} $NaClO_4$ in PC/FEC (PC:FEC = 95:5 in volume)	106.7 mAh·g^{-1} (0.1 C, 2.0–4.0 V)	89% (400 cycles, 2 C, 2.0–4.0 V)	Mitigating the Jahn–Teller effect and suppressing biphasic reactions	[52]
	O3-$Na_{0.93}Ca_{0.035}CrO_2$	Ca^{2+} doping at Cr sites	Solid-state method	1.0 mol·L^{-1} $NaPF_6$ in EC/DEC/FEC (EC:DEC = 1:1 in volume and added 5wt% FEC)	171.9 mAh·g^{-1} (0.1 C, 1.5–3.8 V)	80.3% (1000 cycles, 10 C, 1.5–3.8 V)	Suppressing Cr migration to the Na layer	[63]
	O3-$Na_{0.9}Ca_{0.035}Cr_{0.97}Ti_{0.03}O_2$	Ca^{2+} and Ti^{4+} codoping at Cr sites	Solid-state method	1.0 mol·L^{-1} $NaPF_6$ in EC/DEC/FEC (EC:DEC = 1:1 in volume and added 5wt% FEC)	144.8 mAh·g^{-1} (0.1 C, 1.5–3.8 V)	81.2% (1000 cycles, 10 C, 1.5–3.8 V)	Suppressing the irreversible phase transition	
	P2-$Na_{0.67}Ni_{0.33}Mn_{0.37}Ti_{0.3}O_{1.9}F_{0.1}$	Ti^{4+} doping at Mn sites and F^- doping at O sites	Solid-state method	1.0 mol·L^{-1} $NaClO_4$ in PC/FEC (PC:FEC = 95:5 in volume)	140.3 mAh·g^{-1} (0.1 C, 2.0–4.4 V)	77.2% (300 cycles, 2 C, 2.0–4.4 V)	Suppressing the irreversible phase transition and Na^+/vacancy ordering	[67]
	P2-$K_{0.05}Na_{0.62}MnO_{1.95}F_{0.05}$	K^+ doping at Na sites and F^- doping at O sites	Hydrothermal method followed by sintering	1.0 mol·L^{-1} $NaClO_4$ in EC/DEC/EMC/FEC (EC:DEC:EMC = 1:1:1 in volume and added 5wt% FEC)	210.2 mAh·g^{-1} (0.1 C, 2.0–4.4 V)	73% (100 cycles, 1 C, 2.0–4.4 V)	Suppressing the irreversible phase transition	[68]

Table 1 (Continued)

Method	Cathode material	Strategy details	Synthesis method	Electrolyte	Discharge capacity	Cycling performance	Function	Ref.
Homogeneous surface coating	P2-$Na_{0.66}Mn_{0.9}Mg_{0.1}O_2$@Alucone	Alucone coating	Molecular layer deposition	1.0 mol·L^{-1} $NaClO_4$ in EC/DEC (EC:DEC = 1:1 in volume)	163.1 mAh·g^{-1} (0.1 C, 2.0–4.4 V)	86% (100 cycles, 1 C, 2.0–4.5 V)	Robust nature of the alucone coating	[72]
	P2-$Na_{2/3}Ni_{1/6}Co_{1/6}Mn_{2/3}O_2$@$ZrO_2$	ZrO_2 coating	Coprecipitation followed by sintering	1.0 mol·L^{-1} $NaClO_4$ in PC/FEC (PC:FEC = 19:1 in volume)	140 mAh·g^{-1} (20 mA·g^{-1}, 2.0–4.5 V)	91.4% (100 cycles, 100 mA·g^{-1}, 2.0–4.5 V)	Protecting the electrode from dissolution and stabilizing the SEI film	[73]
	P2-$Na_{2/3}Fe_{1/2}Mn_{1/2}O_2$@$Al_2O_3$	Al_2O_3 coating	Ultrasonic spray pyrolysis followed by sintering	1.0 mol·L^{-1} $NaClO_4$ in PC (PC with 5wt% FEC)	146.7 mAh·g^{-1} (0.1 C, 1.5–4.0 V)	84.7% (40 cycles, 0.1 C, 1.5–4.0 V)	Protecting the electrode from directly contacting with CO_2 and H_2O in air	[75]
	P2-$Na_{0.612}K_{0.056}MnO_2$@$Na_3Zr_2Si_2PO_{12}$	$Na_3Zr_2Si_2PO_{12}$ coating	Wet chemical method	1.0 mol·L^{-1} $NaClO_4$ in PC/FEC (PC:FEC = 95:5 in volume)	203 mAh·g^{-1} (10 mA·g^{-1}, 1.8–4.3 V)	69% (100 cycles, 100 mA·g^{-1}, 1.8–4.3 V)	Alleviating the Jahn–Teller effect and enhancing the Na^+ diffusion coefficient	[76]
	P2-$Na_{2/3}(Mn_{0.54}Ni_{0.13}Co_{0.13})O_2$@$Al_2O_3$	Al_2O_3 coating	Atomic layer deposition	1.0 mol·L^{-1} $NaClO_4$ in EC/DEC (EC:DEC = 1:1 in volume)	124.8 mAh·g^{-1} (1 C, 2.0–4.5 V)	70% (100 cycles, 1 C, 2.0–4.5 V)	Alleviating interface side reactions	[78]
	P2-$Na_{2/3}(Mn_{0.54}Ni_{0.13}Co_{0.13})O_2$@polyimide	Polyimide coating	Wet chemical method	1.0 mol·L^{-1} $NaClO_4$ in EC/DEC (EC:DEC = 1:1 in volume)	151.6 mAh·g^{-1} (1 C, 2.0–4.5 V)	81% (100 cycles, 1 C, 2.0–4.5 V)	Alleviating interface side reactions	
	P2-$Na_{0.67}Li_{0.16}Ni_{0.33}Mn_{0.67}O_{2+\delta}$@PMAA-AN	PMAA-AN coating	Solution polymerization	1.0 mol·L^{-1} $NaPF_6$ in PC/EMC/FEC (EC:DEC = 1:1 in volume and added 4vol% FEC)	173.4 mAh·g^{-1} (0.2 C, 1.5–4.5 V)	73% (300 cycles, 0.5 C, 1.5–4.5 V)	Avoiding transition metal dissolution and interfacial side reactions	[79]
Concentration gradient modification	P2-$Na_{0.65}Ni_{0.16}Co_{0.14}Mn_{0.7}O_2$	Ni, Co, and Mn concentration gradient modification	Coprecipitation followed by sintering	1.0 mol·L^{-1} $NaPF_6$ in EC/DMC/FEC (EC:DMC = 1:1 in volume and added FEC)	162.5 mAh·g^{-1} (30 mA·g^{-1}, 1.5–4.1 V)	51.4% (100 cycles, 83.7 mA·g^{-1}, 1.5–4.1 V)	Providing a structurally stable surface composition	[81]
	O_3-Na[$Ni_{0.6}Co_{0.05}Mn_{0.35}$]$O_2$	Ni-rich core and Mn-rich surface	Coprecipitation followed by sintering	0.5 mol·L^{-1} $NaPF_6$ in EMS/FC (EMS:FC = 98:2 in volume)	157 mAh·g^{-1} (0.1 C, 1.5–4.1 V)	80% (100 cycles, 0.5 C, 1.5–4.1 V)	Reducing the contact area with the electrolyte	[82]
	P2-$Na_{0.67}Ni_{0.167}Co_{0.167}Mn_{0.67}O_2$	Co-rich core and Mn-rich surface	Coprecipitation followed by sintering		142 mAh·g^{-1} (20 mA·g^{-1}, 2.0–4.5 V)	84.5% (100 cycles, 20 mA·g^{-1}, 2.0–4.5 V)	Restricting Ni ion dissolution	[83]
Designing the mixed structure	P2/O3-$Na_{0.85}Mn_{0.5}Ni_{0.4}Fe_{0.1}O_2$	P2/O3 mixed structure	Solid-state method	1.0 mol·L^{-1} $NaPF_6$ in EC/PC (EC:PC = 1:1 in volume)	130 mAh·g^{-1} (0.1 C, 2.0–4.0 V)	86.2% (500 cycles, 1 C, 2.0–4 V)	The survival of the P2 phase during charge and discharge, stabilizing the structure	[86]
	P2/O3-$Na_{0.80}Li_{0.13}Ni_{0.20}Fe_{0.10}Mn_{0.52}O_2$	P2/O3 mixed structure	Solid-state method	1.0 mol·L^{-1} $NaClO_4$ in EC/PC (EC:PC = 1:1 in weight)	180.95 mAh·g^{-1} (0.1 C, 2.0–4.3 V)	93.04% (100 cycles, 1 C, 2.0–4.3 V)	Providing a reversible phase transition and reducing the residual sodium salt on the surface	[87]
	P2/O3-$Na_{0.85}Ni_{0.34}Mn_{0.33}Ti_{0.33}O_2$	P2/O3 mixed structure	Solid-state method	1.0 mol·L^{-1} $NaClO_4$ in PC with 5vol% FEC	126.6 mAh·g^{-1} (0.1 C, 2.2–4.4 V)	80.6% (200 cycles, 1 C, 2.2–4.4 V)	Interlocking effect between the phase boundaries, mitigating the severe structural strain and large lattice volume change	[88]
Particle engineering	O3-$NaNi_{0.5}Mn_{0.5}O_2$	Single-crystal construction	Molten salt method	1.0 mol·L^{-1} $NaClO_4$ in PC with 3wt% FEC	~130 mAh·g^{-1} (0.1 C, 2.0–4.0 V)	69% (200 cycles, 0.2 C, 2.0–4.0 V)	Reducing strain and particle cracking	[89]
	O3-Na($Ni_{0.3}Fe_{0.4}Mn_{0.3}$)O_2	Single-crystal construction	Molten salt method	1.0 mol·L^{-1} $NaClO_4$ in PC with 3wt% FEC	~123 mAh·g^{-1} (0.2 C, 2.0–4.0 V)	76% (100 cycles, 0.2 C, 2.0–4.0 V)	Reducing interfacial side reactions	[90]
	O3-$NaLi_{0.05}Ni_{0.3}Mn_{0.5}Cu_{0.1}Mg_{0.05}O_2$	{010} active facet construction	Thermal polymerization method followed by annealing	1.0 mol·L^{-1} $NaClO_4$ in PC with 5vol% FEC	132.6 mAh·g^{-1} (0.5 C, 2.0–4.0 V)	91.9% (600 cycles, 5 C, 2.0–4.0 V)	Suppressing the unfavorable multiphase transformation in the high voltage regions and retaining a highly reversible O3-P3 phase transition	[92]
	O3-$NaCrO_2$	Submicrospheres	Hydrothermal method	1.0 mol·L^{-1} $NaClO_4$ in EC/DMC (EC:DMC = 1:1 in volume added 1vol% FEC)	118 mAh·g^{-1} (0.2 C, 2.0–3.6 V)	90% (800 cycles, 10 C, 2.0–3.6 V)	Submicrospheres with high structure strength suppressing the stress and strain induced by Na^+ intercalation/deintercalation	[96]

Table 1 (Continued)

Method	Cathode material	Strategy details	Synthesis method	Electrolyte	Discharge capacity	Cycling performance	Function	Ref.
Designing high-entropy material	O3-$NaNi_{0.12}Cu_{0.12}Mg_{0.12}Fe_{0.15}Co_{0.15}Mn_{0.1}Ti_{0.1}Sn_{0.1}Sb_{0.04}O_2$	Nine-component ions in the TM site with varying proportions	Solid-state reaction	1.0 mol·L^{-1} $NaClO_4$ in PC/EC/DMC (PC:EC:DMC = 1:1:1 in volume with 2vol% FEC)	110.3 mAh·g^{-1} (0.1 C, 2.0–3.9 V)	90% (200 cycles, 3 C, 2.0–3.9 V)	Entropy stabilization on the host structure facilitating the O3-type structure to a larger extent and supporting the long-term cycling stability	[102]
	O3-$NaMn_{0.2}Fe_{0.2}Co_{0.2}Ni_{0.2}Ti_{0.2}O_2$	Five-component ions in the TM site with equal proportions	Solid-state method	1.0 mol·L^{-1} $NaPF_6$ in EC/DEC (EC:DEC = 1:1 in volume)	180 mAh·g^{-1} (0.1 C, 1.5–4.2 V)	97% (100 cycles, 0.1 C, 1.5–4.2 V)	Reversible phase transition and the survival of the P3 phase during charge and discharge, stabilizing the structure	[107]
Integrated modification	P2/O3-$Na_{0.7}Mn_{0.4}Ni_{0.3}Cu_{0.1}Fe_{0.1}Ti_{0.1}O_{1.95}F_{0.1}$	P2/O3 mixed structure and designing high-entropy material	Solid-state method	1.0 mol·L^{-1} $NaClO_4$ in PC/FEC (PC:FEC = 95:5 in volume)	133.7 mAh·g^{-1} (20 mA·g^{-1}, 2.0–4.3 V)	88.9% (200 cycles, 200 mA·g^{-1}, 2.0–4.3 V)	Suppressing the Jahn–Teller effect, the destructive sliding of TM layers, and the irreversible P2-O3 phase transition	[108]
	T-CSN6@A	Concentration gradient construction, Ti^{4+} doping, and Al_2O_3 coating	Coprecipitation followed by sintering	1.0 mol·L^{-1} $NaClO_4$ in EC/DMC/FEC (EC:DMC = 1:1 in volume with 5wt% FEC)	163.5 mAh·g^{-1} (0.1 C, 1.5–4.1 V)	85.4% (200 cycles, 0.5 C, 1.5–4.1 V)	Mitigating lattice stress-evoked intergranular cracks and surface side reactions	[109]
	P2-$Na_{0.75}Mn_{0.67}Ni_{0.33}In_{0.02}O$@$NaInO_2$	In^{3+} doping and $NaInO_2$ coating	Coprecipitation followed by sintering	1.0 mol·L^{-1} $NaPF_6$ in EC/DEC	95.4 mAh·g^{-1} (0.1 C, 2.0–4.15 V)	85% (100 cycles, 5 C, 2.0–4.15 V)	In ion serving as a "pillar" to stabilize the structure	[111]

strategies can be summarized as follows: (1) Bulk doping can effectively mitigate the Jahn–Teller effect by regulating the valence state of Mn/Fe, and the doping ion can function as a pillar to stabilize the structure. Meanwhile, interlayer slip, irreversible oxygen loss, and irreversible phase transition can be inhibited by bulk doping. (2) Surface modification can form a protective layer to prevent damage from side reactions. By experimental design, the residual Na content can be converted into a protective layer. Some special coating layers, such as fast ionic conductors and conductive polymers, can also improve ion/electron conduction. (3) Concentration gradient modification builds a special structure providing a stable outer surface and a high-capacity bulk composition. (4) The mixed structure design shows an interlocking effect between phase boundaries, mitigating the severe structural strain and large lattice volume change. (5) Particle engineering can effectively reduce strain and particle cracking because of the special structure of single crystals, active facets, and special morphology. (6) High-entropy material design has attracted wide attention, while the mechanism of remarkable performance is simply due to the entropy stabilization effect or multi-ion synergistic effect. (7) Integrated modification combines the advantages of different modification strategies, and the mechanism of integrated modification is simply due to the synergistic effect of different strategies.

In addition to the abovementioned challenges, other challenges relevant to commercialization should be noted, including insufficient Na^+ in the P2 structure, low operating voltage, and low-temperature performance. First, although the P2 structure shows better stability and an open Na^+ diffusion channel, the insufficient Na^+ reduces its initial charge capacity. This drawback limits the effective specific capacity in the case of matching the anode material without Na^+ [114]. Therefore, an efficient and low-cost presodiation technology is required to promote the development of high-energy SIBs. Second, at low temperatures, the conductivity of the electrolyte and the charge transfer rate at the electrode/electrolyte interface decrease, whereas polarization and dendrites on the anode increase [115]. These problems are factors in the poor performance of applications in extreme environments. In addition, low operating voltage can result in low energy density. Low operating voltage and low-temperature performance can be improved by exploiting electrolytes and optimizing electrode materials.

The challenges, strategies, and perspectives are schematized in Fig. 13. To satisfy the requirements of long-life and high-energy density batteries, efforts devoted to layer oxide cathode materials will never cease. We hope that this review will provide inspiration for the design, synthesis, modification, and application of sodium cathode materials, even in the broader field of materials science.

4.2. Outlook

Recently, the commercialization of SIBs has attracted widespread attention, and great effort has been made to develop layered oxide cathode materials for SIBs, in which cycling performance plays a crucial role. To meet application needs, the following aspects must be investigated:

(1) Clarifying the mechanism of structural degradation and capacity fading: Structural degradation is the main cause of capacity fading for layered oxides, while the degradation mechanism has not been well studied and clarified. The degradation mechanism of cycling performance can be studied using advanced techniques, such as *in-situ* synchrotron X-ray diffraction, the pair distribution function technique, solid-state nuclear magnetic resonance, electron paramagnetic resonance, X-ray absorption spectroscopy, and scanning transmission electron microscopy. For example, *in-situ* synchro-

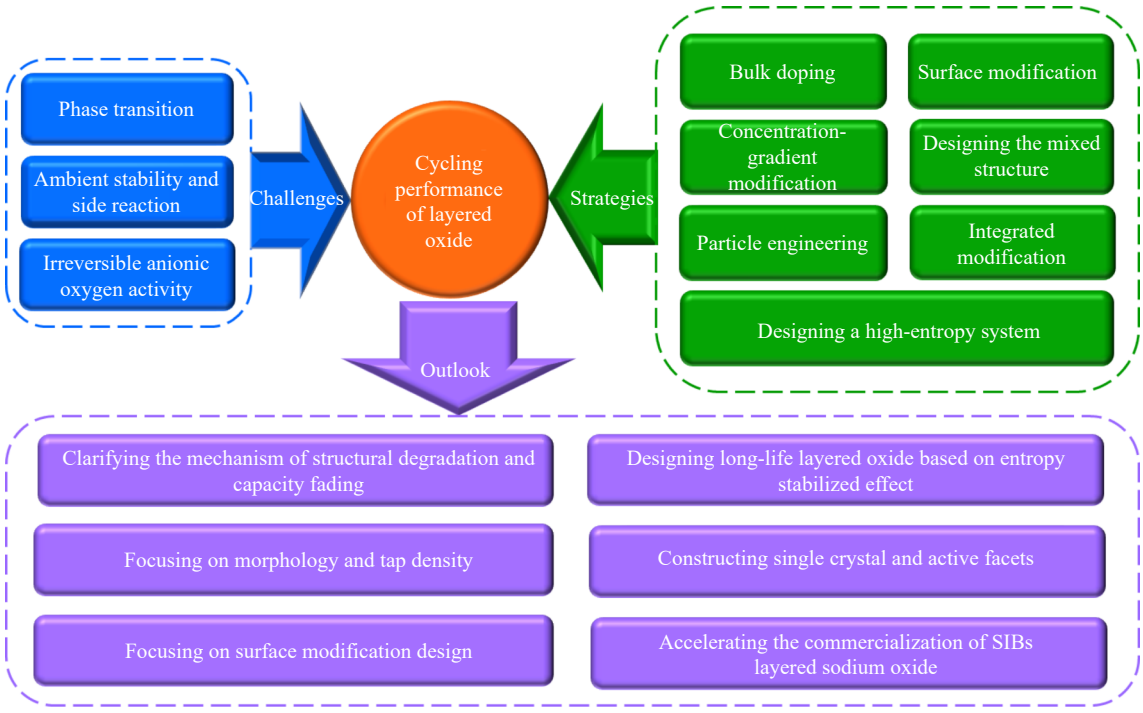

Fig. 13. Summary of the cycling performance of layered oxide cathode materials.

tron X-ray diffraction can provide highly accurate and detailed crystal structure information during charge and discharge, and solid-state nuclear magnetic resonance can reveal the local structural environment, electronic structure, and ion dynamics. This information helps in understanding the degradation mechanism. Moreover, as an important part of the cell, the influence of electrolytes, binders, conductive additives, and separators on structural degradation has always been ignored. The structural change during the cycling process should be clarified in detail with the change in the abovementioned components to reveal the internal reasons for structural degradation and propose the corresponding strategies.

(2) Focusing on morphology and tap density: Particle morphology and tap density are two of the vital factors influencing the energy density and other electrochemical performance aspects of SIBs. However, few reports are available on the morphology and tap density associated with the electrochemical performance of SIB cathodes. Therefore, to achieve higher energy density, various synthesis methods, including coprecipitation and the sol-gel and solvothermal methods, can be tried to optimize the morphology. Meanwhile, energy density does not increase with particle size; energy density and particle size are balanced. Hence, the relationship between energy density and particle size should be studied in detail to optimize electrochemical performance.

(3) Constructing single crystals and active facets: Currently, few reports exist on the construction of single crystals and active facets for layered oxides. Accurate control of the proportion of active facets can improve the Na^+ diffusion kinetics and the degree of cation disorder, so the precursor and sintering process of the single-crystal should be studied in detail. In addition, the relationships between intragranular cracks and phase transition/particle size should be studied to elucidate the mechanism of intragranular crack formation. Moreover, particle engineering integrated with other methods can be tried to exploit high-capacity and long-cycle layered sodium oxides.

(4) Focusing on surface modification design: The side reaction between the cathode and electrolyte leads to the dissolution of transition metals and structural collapse, deteriorating electrochemical performance. A multifunctional surface coating layer can not only mitigate the interphase side reaction but also build a layer with good ionic/electronic conductivity. This multifunctional coating layer can improve cycling performance, discharge capacity, and rate performance. Therefore, how to design the experiment and build a functional coating layer should be further studied.

(5) Designing long-life layered oxides based on the entropy stabilization effect: High-entropy oxides have been a new research interest because of their remarkable properties. However, the improvement in electrochemical performance is simply due to the multi-ion synergy of high-entropy layered oxides, and the mechanism of the entropy stabilization effect remains elusive. Therefore, to fully exploit the potential of high-entropy layered oxides, the mechanism of entropy-dominated phase stabilization effects should be elucidated by revealing the relationships between the high-entropy and phase/particle stability of cathode materials. In addition, the entropy-stabilized effect affects the functional properties of SIBs; therefore, the relationship between entropy and Na^+ diffusion kinetics should be investigated. Moreover, a high-entropy oxide model should be established by high-throughput computational materials engineering and applied to screening suitable elements and contents for the effective design of high-entropy materials.

(6) Accelerating the commercialization of layered oxides for SIBs: At present, research on SIB-layered oxide cathode

materials is nascent. Modification strategies can learn from LIBs, particularly in selecting doped ions, constructing coating layers, designing structures and components, and optimizing morphologies. The discharge capacity of sodium layered oxides is lower than that of lithium-ion cathodes but can be improved by anionic redox reactions. However, it is still unclear how to construct anionic redox in sodium layered oxides and how to maintain a stable structure in the case of anionic redox. The construction of anionic redox reactions and their influence on the reversibility of material structures should be further investigated. Meanwhile, the electrochemical performance of SIBs can be affected by electrolytes, binders, conductive additives, separators, and anode materials; these important cell components should be developed for compatibility with sodium cathode materials. In addition, commercialization challenges, including insufficient Na^+ in the P2 structure, low operating voltage, and low-temperature performance, should be considered. More importantly, the manufacturing process must be further optimized to reduce production costs for a competitive SIB.

Acknowledgements

This work was financially supported by the Fundamental Research Funds for the Central Universities, China (No. 06500177) and the National Natural Science Foundation of China Joint Fund Project (No. U1764255)

Conflict of Interest

Weidong Zhuang is editorial board members for this journal and not involved in the editorial review or the decision to publish this article. All authors declare that they have no financial interests or personal relationships that could have appeared to influence the work reported in this paper.

References

[1] H. Xu, Q. Yan, W.J. Yao, C.S. Lee, and Y.B. Tang, Mainstream optimization strategies for cathode materials of sodium-ion batteries, *Small Struct.*, 3(2022), No. 4, art. No. 2100217.

[2] Y.J. Fang, X.Y. Yu, and X.W. Lou, A practical high-energy cathode for sodium-ion batteries based on uniform P2-$Na_{0.7}CoO_2$ microspheres, *Angew. Chem. Int. Ed.*, 56(2017), No. 21, p. 5801.

[3] J. Wang, Y.F. Yuan, X.H. Rao, *et al*., Realizing high-performance $Na_3V_2(PO4)_2O_2F$ cathode for sodium-ion batteries via Nb-doping, *Int. J. Miner. Metall. Mater.*, 30(2023), No. 10, p. 1859.

[4] C. Delmas, C. Fouassier, and P. Hagenmuller, Structural classification and properties of the layered oxides, *Physica B+C*, 99(1980), No. 1–4, p. 81.

[5] C.L. Zhao, M. Avdeev, L.Q. Chen, and Y.S. Hu, An O3-type Oxide with Low Sodium Content as the Phase-Transition-Free Anode for Sodium-Ion Batteries, *Angew. Chem. Int. Ed.*, 57(2018), No. 24, p. 7056.

[6] C.L. Zhao, Q.D. Wang, Z.P. Yao, *et al*., Rational design of layered oxide materials for sodium-ion batteries, *Science*, 370(2020), No. 6517, p. 708.

[7] X.H. Ma, H.L. Chen, and G. Ceder, Electrochemical properties of monoclinic $NaMnO_2$, *J. Electrochem. Soc.*, 158(2011), No. 12, art. No. A1307.

[8] S. Komaba, T. Nakayama, A. Ogata, *et al*., Electrochemically reversible sodium intercalation of layered $NaNi_{0.5}Mn_{0.5}O_2$ and $NaCrO_2$, *ECS Trans.*, 16(2009), No. 42, p. 43.

[9] N. Yabuuchi, M. Kajiyama, J. Iwatate, *et al*., P2-type $Na_x[Fe_{1/2}Mn_{1/2}]O_2$ made from earth-abundant elements for rechargeable Na batteries, *Nat. Mater.*, 11(2012), No. 6, p. 512.

[10] X.H. Rong, E.Y. Hu, Y.X. Lu, *et al*., Anionic redox reaction-induced high-capacity and low-strain cathode with suppressed phase transition, *Joule*, 3(2019), No. 2, p. 503.

[11] Q. Wang, S. Mariyappan, G. Rousse, *et al*., Unlocking anionic redox activity in O3-type sodium 3d layered oxides via Li substitution, *Nat. Mater.*, 20(2021), No. 3, p. 353.

[12] J.Y. Hwang, J. Kim, T.Y. Yu, and Y.K. Sun, A new P2-type layered oxide cathode with extremely high energy density for sodium-ion batteries, *Adv. Energy Mater.*, 9(2019), No. 15, art. No. 1803346.

[13] Z.H. Wu, Y.X. Ni, S. Tan, *et al*., Realizing high capacity and zero strain in layered oxide cathodes via lithium dual-site substitution for sodium-ion batteries, *J. Am. Chem. Soc.*, 145(2023), No. 17, p. 9596.

[14] F.B. Spingler, M. Naumann, and A. Jossen, Capacity recovery effect in commercial $LiFePO_4$/graphite cells, *J. Electrochem. Soc.*, 167(2020), No. 4, art. No. 040526.

[15] Q.W. Chen, S. Chen, L.L. Zhao, J.Z. Ma, H.S. Wang, and J.T. Zhang, Interface coating of iron nitride on carbon cloth for reversible lithium redox in rechargeable battery, *Chem. Eng. J.*, 431(2022), art. No. 133961.

[16] X.L. Cui, S.M. Wang, X.S. Ye, *et al*., Insights into the improved cycle and rate performance by ex-situ F and *in-situ* Mg dual doping of layered oxide cathodes for sodium-ion batteries, *Energy Storage Mater.*, 45(2022), p. 1153.

[17] W.K. Pang, S. Kalluri, V.K. Peterson, *et al*., Interplay between electrochemistry and phase evolution of the P2-type $Na_x(Fe_{1/2}Mn_{1/2})O_2$ cathode for use in sodium-ion batteries, *Chem. Mater.*, 27(2015), No. 8, p. 3150.

[18] V. Duffort, E. Talaie, R. Black, and L.F. Nazar, Uptake of CO_2 in layered P2-$Na_{0.67}Mn_{0.5}Fe_{0.5}O_2$: Insertion of carbonate anions, *Chem. Mater.*, 27(2015), No. 7, p. 2515.

[19] Y. You, A. Dolocan, W.D. Li, and A. Manthiram, Understanding the air-exposure degradation chemistry at a nanoscale of layered oxide cathodes for sodium-ion batteries, *Nano Lett.*, 19(2019), No. 1, p. 182.

[20] C.L. Xu, H.R. Cai, Q.L. Chen, X.Q. Kong, H.L. Pan, and Y.S. Hu, Origin of air-stability for transition metal oxide cathodes in sodium-ion batteries, *ACS Appl. Mater. Interfaces*, 14(2022), No. 4, p. 5338.

[21] T.Y. Song, C.C. Wang, and C.S. Lee, Structural degradation mechanisms and modulation technologies of layered oxide cathodes for sodium-ion batteries, *Carbon Neutralization*, 1(2022), No. 1, p. 68.

[22] Y. Zhang, M.M. Wu, J.W. Ma, *et al*., Revisiting the $Na_{2/3}Ni_{1/3}Mn_{2/3}O_2$ cathode: Oxygen redox chemistry and oxygen release suppression, *ACS Cent. Sci.*, 6(2020), No. 2, p. 232.

[23] M.D. Jiang, G.N. Qian, X.Z. Liao, *et al*., Revisiting the capacity-fading mechanism of P2-type sodium layered oxide cathode materials during high-voltage cycling, *J. Energy Chem.*, 69(2022), p. 16.

[24] R. House, U. Maitra, L.Y. Jin, *et al*., What triggers oxygen loss in oxygen redox cathode materials?, *Chem. Mater.*, 31(2019), No. 9, p. 3293.

[25] Y.C. Liu, C.C. Wang, S. Zhao, *et al*., Mitigation of Jahn–Teller distortion and Na^+/vacancy ordering in a distorted manganese oxide cathode material by Li substitution, *Chem. Sci.*, 12(2021), No. 3, p. 1062.

[26] L.J. Wang, Y.Z. Wang, J.B. Zhao, Y.H. Li, J.L. Wang, and X.H. Yang, Nb^{5+}-doped P2-type Mn-based layered oxide cathode with an excellent high-rate cycling stability for sodium-ion batteries, *Ionics*, 25(2019), No. 10, p. 4775.

[27] J.L. Zhang, J.B. Kim, J. Zhang, *et al*., Regulating Pseudo–Jahn–Teller effect and superstructure in layered cathode materials for reversible alkali-ion intercalation, *J. Am. Chem. Soc.*, 144(2022), No. 17, p. 7929.

[28] J.L. Zhang, W.H. Wang, W. Wang, S.W. Wang, and B.H. Li, Comprehensive review of P2-type $Na_{2/3}Ni_{1/3}Mn_{2/3}O_2$, a potential cathode for practical application of Na-ion batteries, *ACS Appl. Mater. Interfaces*, 11(2019), No. 25, p. 22051.

[29] Y.L. Liu, D. Wang, H.Y. Li, *et al*., Research progress in O3-type phase Fe/Mn/Cu-based layered cathode materials for sodium ion batteries, *J. Mater. Chem. A*, 10(2022), No. 8, p. 3869.

[30] H. Fang, H.C. Ji, J.J. Zhai, *et al*., Mitigating jahn–teller effect in layered cathode material via interstitial doping for high-performance sodium-ion batteries, *Small*, 19(2023), No. 35, art. No. 2301360.

[31] X.H. Yang, Y.Z. Wang, J.L. Wang, J.Y. Deng, and X. Zhang, Superior cyclability of Ce-doped P2-$Na_{0.67}Co_{0.20}Mn_{0.80}O_2$ cathode for sodium storage, *J. Phys. Chem. Solids*, 148(2021), art. No. 109750.

[32] W.C. Qin, Y. Liu, J.F. Liu, Z.H. Yang, and Q.Q. Liu, Boosting the ionic transport and structural stability of Zn-doped O3-type $NaNi_{1/3}Mn_{1/3}Fe_{1/3}O_2$ cathode material for half/full sodium-ion batteries, *Electrochim. Acta*, 418(2022), art. No. 140357.

[33] L. Zhang, T. Yuan, L.K. Soule, *et al*., Enhanced ionic transport and structural stability of Nb-doped O3-$NaFe_{0.55}Mn_{0.45-x}Nb_xO_2$ cathode material for long-lasting sodium-ion batteries, *ACS Appl. Energy Mater.*, 3(2020), No. 4, p. 3770.

[34] H. Zhao, J.Z. Li, W.P. Liu, *et al*., Integrated titanium-substituted air stable O3 sodium layered oxide electrode via a complexant assisted route for high capacity sodium-ion battery, *Electrochim. Acta*, 388(2021), art. No. 138561.

[35] Y.H. Feng, Z.W. Cheng, C.L. Xu, *et al*., Low-cost Al-doped layered cathodes with improved electrochemical performance for rechargeable sodium-ion batteries, *ACS Appl. Mater. Interfaces*, 14(2022), No. 20, p. 23465.

[36] J. Feng, S.H. Luo, J.C. Wang, *et al*., Stable electrochemical properties of magnesium-doped co-free layered P2-type $Na_{0.67}Ni_{0.33}Mn_{0.67}O_2$ cathode material for sodium ion batteries, *ACS Sustainable Chem. Eng.*, 10(2022), No. 15, p. 4994.

[37] W. Ko, M.K. Cho, J. Kang, *et al*., Exceptionally increased reversible capacity of O3-type $NaCrO_2$ cathode by preventing irreversible phase transition, *Energy Storage Mater.*, 46(2022), p. 289.

[38] Y.F. Wen, J.J. Fan, C.G. Shi, *et al*., Probing into the working mechanism of Mg versus Co in enhancing the electrochemical performance of P2-Type layered composite for sodium-ion batteries, *Nano Energy*, 60(2019), p. 162.

[39] G.Q. Su, L.J. Li, Z. Shi, X.B. Ma, L. Ma, and Z.J. Cao, Boosting anionic redox through lithium doping in P2-layered cathode for high-performance sodium-ion batteries, *Appl. Surf. Sci.*, 608(2023), art. No. 155097.

[40] L.J. Li, G.Q. Su, C. Lu, *et al*., Effect of lithium doping in P2-Type layered oxide cathodes on the electrochemical performances of Sodium-Ion batteries, *Chem. Eng. J.*, 446(2022), art. No. 136923.

[41] Z.Y. Li, X.B. Ma, K. Sun, L.F. He, Y.Q. Li, and D.F. Chen, $Na_{2/3}Li_{1/9}[Ni_{2/9}Li_{1/9}Mn_{2/3}]O_2$: A high-performance solid-solution reaction layered oxide cathode material for sodium-ion batteries, *ACS Appl. Energy Mater.*, 5(2022), No. 1, p. 1126.

[42] Q. Huang, M.Y. Wang, L. Zhang, *et al*., Shear-resistant interface of layered oxide cathodes for sodium ion batteries, *Energy Storage Mater.*, 45(2022), p. 389.

[43] L.T. Yang, L.Y. Kuo, J.M. López del Amo, *et al*., Structural aspects of P2-type $Na_{0.67}Mn_{0.6}Ni_{0.2}Li_{0.2}O_2$ (MNL) stabilization by lithium defects as a cathode material for sodium-ion batteries, *Adv. Funct. Mater.*, 31(2021), No. 38, art. No. 2102939.

[44] Y.S. Wang, Z.M. Feng, P.X. Cui, *et al*., Pillar-beam structures prevent layered cathode materials from destructive phase transitions, *Nat. Commun.*, 12(2021), No. 1, art. No. 13.

[45] C.C. Wang, L.J. Liu, S. Zhao, *et al*., Tuning local chemistry of P2 layered-oxide cathode for high energy and long cycles of sodium-ion battery, *Nat. Commun.*, 12(2021), No. 1, art. No. 2256.

[46] G.X. Tang, Z.W. Chen, Z.Y. Lin, *et al*., K^+-doped P2-$Na_{0.67}Fe_{0.5}Mn_{0.5}O_2$ cathode for highly enhanced rate performance sodium-ion battery, *J. Alloys Compd.*, 947(2023), art. No. 169482.

[47] X.Y. Li, J.Z. Miao, H.W. Long, *et al*., Sodium-storage performance of K^+-intercalated $Na_xCu_{0.2}Mn_{0.8}O_2$, *ACS Appl. Energy Mater.*, 5(2022), No. 3, p. 2758.

[48] Q. Zhang, Y.Y. Huang, Y. Liu, *et al*., F-doped O_3-$NaNi_{1/3}Fe_{1/3}Mn_{1/3}O_2$ as high-performance cathode materials for sodium-ion batteries, *Sci. China Mater.*, 60(2017), No. 7, p. 629.

[49] H.L. Hu, H.C. He, R.K. Xie, *et al*., Achieving reversible Mn^{2+}/Mn^{4+} double redox couple through anionic substitution in a P2-type layered oxide cathode, *Nano Energy*, 99(2022), art. No. 107390.

[50] G.L. Liu, W.L. Xu, J.H. Wu, *et al*., Unlocking high-rate O3 layered oxide cathode for Na-ion batteries via ion migration path modulation, *J. Energy Chem.*, 83(2023), p. 53.

[51] S.Q. Liu, B.Y. Wang, X. Zhang, S. Zhao, Z.H. Zhang, and H.J. Yu, Reviving the lithium-manganese-based layered oxide cathodes for lithium-ion batteries, *Matter*, 4(2021), No. 5, p. 1511.

[52] K. Liu, S.S. Tan, J. Moon, *et al*., Insights into the enhanced cycle and rate performances of the F-substituted P2-type oxide cathodes for sodium-ion batteries, *Adv. Energy Mater.*, 10(2020), No. 19, art. No. 2000135.

[53] H. Chen, Z.G. Wu, Y.J. Zhong, *et al*., Boosting the reactivity of Ni^{2+}/Ni^{3+} redox couple *via* fluorine doping of high performance $Na_{0.6}Mn_{0.95}Ni_{0.05}O_{2-x}F_x$ cathode, *Electrochim. Acta*, 308(2019), p. 64.

[54] C.J. Zhou, L.C. Yang, C.G. Zhou, *et al*., Fluorine-substituted O3-type $NaNi_{0.4}Mn_{0.25}Ti_{0.3}Co_{0.05}O_{2-x}F_x$ cathode with improved rate capability and cyclic stability for sodium-ion storage at high voltage, *J. Energy Chem.*, 60(2021), p. 341.

[55] W.P. Kang, P. Ma, Z.N. Liu, *et al*., Tunable electrochemical activity of P2-$Na_{0.6}Mn_{0.7}Ni_{0.3}O_{2-x}F_x$ microspheres as high-rate cathodes for high-performance sodium ion batteries, *ACS Appl. Mater. Interfaces*, 13(2021), No. 13, p. 15333.

[56] S.Y. Chu, D. Kim, G. Choi, *et al*., Revealing the origin of transition-metal migration in layered sodium-ion battery cathodes: Random Na extraction and Na-free layer formation, *Angew. Chem. Int. Ed.*, 62(2023), No. 12, art. No. e202216174.

[57] H.R. Yao, P.F. Wang, Y. Gong, *et al*., Designing air-stable O_3-type cathode materials by combined structure modulation for Na-ion batteries, *J. Am. Chem. Soc.*, 139(2017), No. 25, p. 8440.

[58] H.R. Shi, J.Y. Li, M.J. Liu, *et al*., Multiple strategies toward advanced P2-type layered Na_xMnO_2 for low-cost sodium-ion batteries, *ACS Appl. Energy Mater.*, 4(2021), No. 8, p. 8183.

[59] R. Qi, M.H. Chu, W.G. Zhao, *et al*., A highly-stable layered Fe/Mn-based cathode with ultralow strain for advanced sodium-ion batteries, *Nano Energy*, 88(2021), art. No. 106206.

[60] Q. Liu, W. Zheng, G.Y. Liu, *et al*., Realizing high-performance cathodes with cationic and anionic redox reactions in high-sodium-content P2-type oxides for sodium-ion batteries, *ACS Appl. Mater. Interfaces*, 15(2023), No. 7, p. 9324.

[61] G.Q. Su, H.Q. Zheng, H. Chen, and S. Bao, Ca/Mg dual-doping P2-type $Na_{0.67}Ni_{0.17}Co_{0.17}Mn_{0.66}O_2$ cathode material for so-

dium ion batteries, *Mater. Lett.*, 331(2023), art. No. 133425.
[62] K. Kubota, T. Asari, and S. Komaba, Impact of Ti and Zn dual-substitution in P2 type $Na_{2/3}Ni_{1/3}Mn_{2/3}O_2$ on Ni–Mn and Na-vacancy ordering and electrochemical properties, *Adv. Mater.*, 35(2023), No. 26, art. No. 2300714.
[63] I. Lee, G. Oh, S. Lee, *et al*., Cationic and transition metal co-substitution strategy of O_3-type $NaCrO_2$ cathode for high-energy sodium-ion batteries, *Energy Storage Mater.*, 41(2021), p. 183.
[64] T.L. Zhang, H.C. Ji, X.H. Hou, *et al*., Promoting the performances of P2-type sodium layered cathode by inducing Na site rearrangement, *Nano Energy*, 100(2022), art. No. 107482.
[65] Y.X. Zhang, G.Q. Liu, C. Su, *et al*., Study on the influence of Cu/F dual-doping on the Fe–Mn based compound as cathode material for sodium ion batteries, *J. Power Sources*, 536(2022), art. No. 231511.
[66] M.S. Chae, H.J. Kim, J. Lyoo, *et al*., Anomalous sodium storage behavior in Al/F dual-doped P2-type sodium manganese oxide cathode for sodium-ion batteries, *Adv. Energy Mater.*, 10(2020), No. 43, art. No. 2002205.
[67] P.F. Zhou, J. Zhang, Z.N. Che, *et al*., Insights into the enhanced structure stability and electrochemical performance of Ti^{4+}/F^- co-doped P2-$Na_{0.67}Ni_{0.33}Mn_{0.67}O_2$ cathodes for sodium ion batteries at high voltage, *J. Energy Chem.*, 67(2022), p. 655.
[68] R.H. Nie, H.X. Chen, Y.T. Yang, C. Li, and H.M. Zhou, High-voltage layered manganese-based oxide cathode with excellent rate capability enabled by K/F co-doping, *ACS Appl. Energy Mater.*, 6(2023), No. 4, p. 2358.
[69] B. Peng, G.L. Wan, N. Ahmad, L. Yu, X.Y. Ma, and G.Q. Zhang, Recent progress in the emerging modification strategies for layered oxide cathodes toward practicable sodium ion batteries *Adv. Energy Mater*., 13(2023), No. 27, art. No. 2300334.
[70] L.Y. Yang, S.W. Sun, K. Du, *et al*., Prompting structure stability of O3-$NaNi_{0.5}Mn_{0.5}O_2$ *via* effective surface regulation based on atomic layer deposition, *Ceram. Int.*, 47(2021), No. 20, p. 28521.
[71] M.Z. Leng, J.Q. Bi, W.L. Wang, *et al*., Ultrathin MgO coating on fabricated O3-$NaNi_{0.45}Mn_{0.3}Ti_{0.2}Zr_{0.05}O_2$ composite cathode via magnetron sputtering for enhanced kinetic and durable sodium-ion batteries, *J. Alloys Compd.*, 855(2021), art. No. 157533.
[72] K. Kaliyappan, T. Or, Y.P. Deng, Y.F. Hu, Z.Y. Bai, and Z.W. Chen, Constructing safe and durable high-voltage P2 layered cathodes for sodium ion batteries enabled by molecular layer deposition of alucone, *Adv. Funct. Mater.*, 30(2020), No. 17, art. No. 1910251.
[73] S. Bao, S.H. Luo, and J.L. Lu, Preparation and optimization of ZrO_2 modified P2-type $Na_{2/3}Ni_{1/6}Co_{1/6}Mn_{2/3}O_2$ with enhanced electrochemical performance as cathode for sodium ion batteries, *Ceram. Int.*, 46(2020), No. 10, p. 16080.
[74] Y.Z. Wang and J.T. Tang, CeO_2-modified P2-Na–Co–Mn–O cathode with enhanced sodium storage characteristics, *RSC Adv.*, 8(2018), No. 43, p. 24143.
[75] Y.J. Chang, G.H. Xie, Y.M. Zhou, *et al*., Enhancing storage performance of P2-type $Na_{2/3}Fe_{1/2}Mn_{1/2}O_2$ cathode materials by Al_2O_3 coating, *Trans. Nonferrous Met. Soc. China*, 32(2022), No. 1, p. 262.
[76] Y.Q. Shao, X.X. Wang, B.C. Li, *et al*., Functional surface modification of P2-type layered Mn-based oxide cathode by thin layer of NASICON for sodium-ion batteries, *Electrochim. Acta*, 442(2023), art. No. 141915.
[77] D. Lu, Z.J. Yao, Y. Zhong, *et al*., Polypyrrole-coated sodium manganate hollow microspheres as a superior cathode for sodium ion batteries, *ACS Appl. Mater. Interfaces*, 11(2019), No. 17, p. 15630.
[78] K. Kaliyappan, G.R. Li, L. Yang, Z.Y. Bai, and Z.W. Chen, An ion conductive polyimide encapsulation: New insight and significant performance enhancement of sodium based P2 layered cathodes, *Energy Storage Mater.*, 22(2019), p. 168.
[79] J.L. Lin, Q. Huang, K. Dai, *et al*., Mitigating interfacial instability of high-voltage sodium layered oxide cathodes with coordinative polymeric structure, *J. Power Sources*, 552(2022), art. No. 232235.
[80] T.C. Liu, L. Yu, J. Lu, *et al*., Rational design of mechanically robust Ni-rich cathode materials via concentration gradient strategy, *Nat. Commun.*, 12(2021), No. 1, art. No. 6024.
[81] N.S. Gao, Y.W. Guo, Y.H. Chen, *et al*., Improved electrochemical performance of P2-type concentration-gradient cathode material $Na_{0.65}Ni_{0.16}Co_{0.14}Mn_{0.7}O_2$ with Mn-rich core for sodium-ion batteries, *J. Alloys Compd.*, 958(2023), art. No. 170386.
[82] J.Y. Hwang, S.M. Oh, S.T. Myung, K.Y. Chung, I. Belharouak, and Y.K. Sun, Radially aligned hierarchical columnar structure as a cathode material for high energy density sodium-ion batteries, *Nat. Commun.*, 6(2015), art. No. 6865.
[83] S. Bao, S.H. Luo, Z.Y. Wang, S.X. Yan, Q. Wang, and J.Y. Li, Novel P2-type concentration-gradient $Na_{0.67}Ni_{0.167}Co_{0.167}Mn_{0.67}O_2$ modified by Mn-rich surface as cathode material for sodium ion batteries, *J. Power Sources*, 396(2018), p. 404.
[84] S.H. Guo, Q. Li, P. Liu, M.W. Chen, and H.S. Zhou, Environmentally stable interface of layered oxide cathodes for sodium-ion batteries, *Nat. Commun.*, 8(2017), No. 1, art. No. 135.
[85] C. Hakim, H.D. Asfaw, R. Younesi, D. Brandell, K. Edström, and I. Saadoune, Development of P2 or P2/P3 cathode materials for sodium-ion batteries by controlling the Ni and Mn contents in $Na_{0.7}Co_xMn_yNi_zO_2$ layered oxide, *Electrochim. Acta*, 438(2023), art. No. 141540.
[86] B.W. Xiao, X. Liu, M. Song, *et al*., A general strategy for batch development of high-performance and cost-effective sodium layered cathodes, *Nano Energy*, 89(2021), art. No. 106371.
[87] J.M. Feng, D. Fang, Z. Yang, *et al*., A novel P2/O3 composite cathode toward synergistic electrochemical optimization for sodium ion batteries, *J. Power Sources*, 553(2023), art. No. 232292.
[88] L.Z. Yu, Z.W. Cheng, K. Xu, *et al*., Interlocking biphasic chemistry for high-voltage P2/O3 sodium layered oxide cathode, *Energy Storage Mater.*, 50(2022), p. 730.
[89] J. Darga and A. Manthiram, Facile synthesis of O3-type $NaNi_{0.5}Mn_{0.5}O_2$ single crystals with improved performance in sodium-ion batteries, *ACS Appl. Mater. Interfaces*, 14(2022), No. 47, p. 52729.
[90] J. Lamb, K. Jarvis, and A. Manthiram, Molten-salt synthesis of O3-Type layered oxide single crystal cathodes with controlled morphology towards long-life sodium-ion batteries, *Small*, 18(2022), No. 43, art. No. 2106927.
[91] B. Peng, Z.H. Zhou, J. Xu, *et al*., Crystal facet design in layered oxide cathode enables low-temperature sodium-ion batteries, *ACS Materials Lett.*, 5(2023), No. 8, p. 2233.
[92] Y. Xiao, P.F. Wang, Y.X. Yin, *et al*., Exposing{010}active facets by multiple-layer oriented stacking nanosheets for high-performance capacitive sodium-ion oxide cathode, *Adv. Mater.*, 30(2018), No. 40, art. No. 1803765.
[93] F.P. Zhang, Y. Lu, Y. Guo, *et al*., Highly stabilized single-crystal P2-type layered oxides obtained via rational crystal orientation modulation for sodium-ion batteries, *Chem. Eng. J.*, 458(2023), art. No. 141515.
[94] N. Bucher, S. Hartung, A. Nagasubramanian, Y.L. Cheah, H.E. Hoster, and S. Madhavi, Layered Na_xMnO_{2+z} in sodium ion batteries-influence of morphology on cycle performance, *ACS Appl. Mater. Interfaces*, 6(2014), No. 11, p. 8059.
[95] K. Kaliyappan, W. Xaio, T.K. Sham, and X.L. Sun, High tap

density co and Ni containing P2-$Na_{0.66}MnO_2$ buckyballs: A promising high voltage cathode for stable sodium-ion batteries, *Adv. Funct. Mater.*, 28(2018), No. 32, art. No. 1801898.

[96] S. Wang, F. Chen, X.D. He, *et al*., Self-template synthesis of $NaCrO_2$ submicrospheres for stable sodium storage, *ACS Appl. Mater. Interfaces*, 13(2021), No. 10, p. 12203.

[97] Y.C. Liu, Q.Y. Shen, X.D. Zhao, *et al*., Hierarchical engineering of porous P2-$Na_{2/3}Ni_{1/3}Mn_{2/3}O_2$ nanofibers assembled by nanoparticles enables superior sodium-ion storage cathodes, *Adv. Funct. Mater.*, 30(2020), No. 6, art. No. 1907837.

[98] L.W. Liang, X. Sun, D.K. Denis, *et al*., Ultralong layered $NaCrO_2$ nanowires: A competitive wide-temperature-operating cathode for extraordinary high-rate sodium-ion batteries, *ACS Appl. Mater. Interfaces*, 11(2019), No. 4, p. 4037.

[99] S. Kalluri, K.H. Seng, W.K. Pang, *et al*., Electrospun P2-type $Na_{2/3}(Fe_{1/2}Mn_{1/2})O_2$ hierarchical nanofibers as cathode material for sodium-ion batteries, *ACS Appl. Mater. Interfaces*, 6(2014), No. 12, p. 8953.

[100] M.J. Aragón, P. Lavela, G. Ortiz, R. Alcántara, and J.L. Tirado, Nanometric P2-$Na_{2/3}Fe_{1/3}Mn_{2/3}O_2$ with controlled morphology as cathode for sodium-ion batteries, *J. Alloys Compd.*, 724(2017), p. 465.

[101] J. Molenda, A. Milewska, W. Zając, *et al*., Impact of O3/P3 phase transition on the performance of the $Na_xTi_{1/6}Mn_{1/6}Fe_{1/6}Co_{1/6}Ni_{1/6}Cu_{1/6}O_2$ cathode material for Na-ion batteries, *J. Mater. Chem. A*, 11(2023), No. 8, p. 4248.

[102] C.L. Zhao, F.X. Ding, Y.X. Lu, L.Q. Chen, and Y.S. Hu, High-entropy layered oxide cathodes for sodium-ion batteries, *Angew. Chem. Int. Ed.*, 59(2020), No. 1, p. 264.

[103] Z.Y. Gu, J.Z. Guo, J.M. Cao, *et al*., An advanced high-entropy fluorophosphate cathode for sodium-ion batteries with increased working voltage and energy density, *Adv. Mater.*, 34(2022), No. 14, art. No. 2110108.

[104] B.S. Murty, J.W. Yeh, and S. Ranganathan, *High Entropy Alloys*, Butterworth-Heinemann, Oxford, 2014.

[105] A. Sarkar, Q.S. Wang, A. Schiele, *et al*., High-entropy oxides: Fundamental aspects and electrochemical properties, *Adv. Mater.*, 31(2019), No. 26, art. No. 1806236.

[106] G. Anand, A.P. Wynn, C.M. Handley, and C.L. Freeman, Phase stability and distortion in high-entropy oxides, *Acta Mater.*, 146(2018), p. 119.

[107] K. Walczak, A. Plewa, C. Ghica, *et al*., $NaMn_{0.2}Fe_{0.2}Co_{0.2}Ni_{0.2}Ti_{0.2}O_2$ high-entropy layered oxide–experimental and theoretical evidence of high electrochemical performance in sodium batteries, *Energy Storage Mater.*, 47(2022), p. 500.

[108] P.F. Zhou, Z.N. Che, J. Liu, *et al*., High-entropy P2/O3 biphasic cathode materials for wide-temperature rechargeable sodium-ion batteries, *Energy Storage Mater.*, 57(2023), p. 618.

[109] W.L. Xu, R.B. Dang, L. Zhou, *et al*., Conversion of surface residual alkali to solid electrolyte to enable Na-ion full cells with robust interfaces, *Adv. Mater.*, 35(2023), No. 42, art. No. 2301314.

[110] X.Y. Li, L.W. Liang, M.S. Su, *et al*., Multi-level modifications enabling chemomechanically stable Ni-rich O3-Layered cathode toward wide-temperature-tolerance quasi-solid-state Na-ion batteries, *Adv. Energy Mater.*, 13(2023), No. 9, art. No. 2203701.

[111] X.C. Feng, Y. Li, Q.H. Shi, *et al*., A comprehensive modification enables the high rate capability of P2-$Na_{0.75}Mn_{0.67}Ni_{0.33}O_2$ for sodium-ion cathode materials, *J. Energy Chem.*, 69(2022), p. 442.

[112] S.Y. Zhao, Q.H. Shi, R.J. Qi, *et al*., $NaTi_2(PO_4)_3$ modified O3-type $NaNi_{1/3}Fe_{1/3}Mn_{1/3}O_2$ as high rate and air stable cathode for sodium-ion batteries, *Electrochim. Acta*, 441(2023), art. No. 141859.

[113] H.B. Wang, F.X. Ding, Y.Q. Wang, *et al.*, *In situ* plastic-crystal-coated cathode toward high-performance Na-ion batteries, *ACS Energy Lett.*, 8(2023), No. 3, p. 1434.

[114] M.L. Xu, M.C. Liu, Z.Z. Yang, C. Wu, and J.F. Qian, Research progress on presodiation strategies for high energy sodium-ion batteries, *Acta Phys. Chim. Sin.*, 39(2023), No. 3, art. No. 2210043.

[115] P.Y. Li, N.Q. Hu, J.Y. Wang, S.C. Wang, and W.W. Deng, Recent progress and perspective: Na ion batteries used at low temperatures, *Nanomaterials*, 12(2022), No. 19, art. No. 3529.